Bragg Grating Integrated on Silicon-on-Insulator Waveguide

Bragg Grating Integrated on Silicon-on-Insulator Waveguide

By

HAO WANG

B. Eng. (Shanghai University) 2001

A Thesis
Submitted to the School of Graduate Studies
in Partial Fulfilment of the Requirements
for the Degree
Master of Applied Science

McMaster Unviersity

MASTER OF APPLIED SCIENCE (2003) McMaster University
(Engineering Physics) Hamilton, Ontario

TITLE: Bragg Grating Integrated on Silicon-on-Insulator Waveguide

AUTHOR: Hao Wang, B. Eng. (Shanghai University)

SUPERVISOR: Dr. Paul Jessop

NUMBER OF PAGES: ix, 78

Abstract

This thesis details the design, fabrication and measurement of an integrated optical Bragg grating filter, operating at a free space wavelength of 1532 nm, based on silicon-on-insulator (SOI) ridge waveguide.

Grating-based integrated devices can interact with optical signals in photonic integrated circuits (PIC) in such a way as to selectively transmit, reflect or detect the signals that are resonant with these devices. Channel filters can access one channel of a wavelength division multiplexed signal without disturbing the other channels and are therefore important elements in WDM communications. Resonator filters are attractive candidates because they can potentially realize the narrowest linewidth for a given device size.

Device models for this kind of device are developed by using the MATLAB programming language. Coupled mode theory (CMT) for filters, and the effective index method (EIM) which reduces a three dimensional (3D) analysis into two dimensions is used as modeling theoretical background. Computer modeling identifies the effect of device structure on the performance of the devices, and is also used to predict the output characteristics of this kind of device. This provides an understanding of device physics and operation, and a basis for comparison with experimental results.

A common fabrication sequence for integrated optical Bragg grating filters based on SOI ridge waveguides is designed, developed and demonstrated. This includes the photomask for optical ridged waveguide, interferometic lithography for grating pattern and high accuracy RIE etching.

This work demonstrates Bragg grating as a technology for realizing PIC in SOI material system, and presents the technology required to design, fabricate, characterize, and model these integrated devices.

Acknowledgements

First of all, I want to extend my sincere gratitude to my supervisor, Dr. Paul Jessop, for his time, advice, insight and guidance during my Master study.

I would like to thank Dr. Doug Bruce for the cleanroom help, advices in planning the fabrication and setting up testing experiments in the lab.

I also would like to give thanks to my other colleagues at the Center for Electronphotonic Materials & Devices: Dr. Weihong Jiang, Dr. Daizong Li for training grating processing and their suggestions and discussion for my research work; Dr. Zhilin Peng for his assistance in clean room. I am grateful to Andy Duft whom I often made overworked. Contributed greatly to his excellent job and experience for doing AFM measurements, I can present wonderful AFM images in my thesis which is very important in my research work. Here, I want to make my special thanks to Graham Pearson, one of my best friends, who helped me a lot in the lab. Also summer student, Grant, without his help in programming the software of Labview controlling system, the test and analysis work would have been much more difficult.

Finally, I would like to thank my parents for their many years support throughout all aspects of my life. Without their moral support, useful suggestions, constant encouragements and financial support, the completion of this work would not have been possible.

Contents

List of Figures

List of Tables

CHAPTER 1 INTRODUCTION

1.1 Overview

During the past decade, the world has seen an explosive growth in optical telecommunications, fueled in part by the rapid expansion of the Internet. Not only are optical telecommunications systems constantly improving in their performance and capacity, but the deployment of optical systems is spreading deeper into the consumer market. Fiber optic networks will be routed directly into neighborhoods, households, and even to the back of each computer. [1] In the more distant future, it is possible that even the signals bouncing between the different components inside the computer will be transmitted and received optically. As optical fiber gradually replaces copper cables, it will become necessary for many of the electronic network components to be replaced by equivalent optical components: splitters, filters, routers, and switches.

In order for these optical components to be compact, manufacturable, low cost, and integratable, it is highly desirable that they be fabricated on a planar surface. The concept of integrated optics has existed since 1969 when a complete work of waveguide analysis and design of waveguide bends and filters was presented [2]. However, it is only recently that favorable conditions for the development of this technology have emerged. The bandwidth requirements for internet services and the promise of high bandwidth links to homes are driving the development of high data rate communication systems. Wavelength division multiplexing (WDM), which is the main approach to increasing the capacity of optical fibers, relies heavily on devices for efficient signal processing at the optical level, thus creating a need for low cost high performance integrated optical devices. With channel spacing of 100GHz and higher becoming standard for long haul communications, there is a requirement for

high performance filters to maintain channel separation. The wider the filter bandwidth, the less stringent are the tolerances for its center frequency and the less the sensitivity of filter performance to environmental changes.

The minimum size of integrated optics devices depends on the dielectric contrast of the layers used to form the components. High index contrast (HIC) waveguides have a high index core and a low index cladding. Examples of HIC material systems with the advantage that they are compatible with silicon ULSI processing are strip waveguide of silicon (Si) or silicon nitride (Si_3N_4), on a silicon dioxide (SiO_2) substrate with air or SiO_2 cladding. The index differences of 2-2.5 and 0.5-1 , respectively are much larger than those of typical wave guiding systems, such as optical fibers or doped silica waveguides, which have index differences as small as 0.01. HIC waveguides are characterized by stronger light confinement. Thus, abrupt changes in the light flow can be achieved very efficiently in a very small area, and HIC waveguides have much smaller cross section dimensions than the above mentioned ordinary fiber wave guiding systems, which have cross sectional dimensions on the order of $10\times10\mu m^2$. They also tend to have stronger polarization dependence, greater scattering loss caused by surface roughness, and connection to fibers is much more difficult. Of great importance is also the ability to couple light efficiently into and out of the photonic integrated circuits (PIC), which is a very challenging task due to the large mode mismatch between fibers and integrated waveguides. Moreover, because of the miniature size of such devices, even a high dB/cm loss corresponds to a low overall loss, allowing the dense integration of optical devices on a chip. [3]

The devices examined in this thesis are Bragg gratings for wavelength filtering based on silicon on insulator (SOI) material system. Such devices are essential

components of photonic integrated circuits (PIC). This thesis not only describes the fabrication and characterization of an integrated Bragg grating on silicon on insulator ridge waveguide, but also demonstrates the computer simulation transmission spectra of this promising new wavelength filtering device. To our knowledge, this is the first time to use computer simulation to predict resonance frequency of Bragg grating filter, and the experimental results can well agree with the computer simulation.

1.2 Structure of This Thesis

Chapter 1 of this thesis presents the theory relevant to optical waveguides. Mode solutions for asymmetric waveguides are presented and discussed. Chapter 2 describes the silicon on insulator (SOI) material system. Single mode conditions and calculations for SOI waveguides are discussed and explained. Modeling methods such as effective index method (EIM) and beam propagation method (BPM) are reviewed. Chapter 3 discusses the coupled mode theory (CMT) and derives the equation for coupling coefficient κ, which is very important to analyze energy exchange between two modes. Detailed grating fabrication techniques are presented in chapter 4, and a specific experimental fabrication recipe for Bragg grating on SOI is also discussed. Characterization techniques and personal skills are also reported in this chapter. Chapter 5 presents experimental setup and results illustrating the filter performance. Higher order dips and loss mechanisms are also discussed. Chapter 6 utilizes computer simulation to explore all the grating parameters and comes up with optimization designs. Chapter 7 summarizes the results drawn from this project, and briefly discusses future research.

1.3 Introduction to Optical Waveguides

Optical waveguides connect various parts of an optical circuit, just as metallic strips connect various electrical components on an integrated circuit. However, optical waves travel in the waveguide in distinct optical modes, with spatial distribution of optical energy that is confined to the area near the waveguide core. This waveguide is produced by varying the refractive index of the material such that the core has a higher index than the cladding layers on either side. A brief review of the physics of wave propagation in materials is given here, and a more detailed derivation can be found in [4].

The behavior of electromagnetic waves in matter can be determined by a set of partial differential equation called Maxwell's equations,

$$\nabla \times \vec{E} = -\frac{d\vec{B}}{dt} \qquad (1.1)$$

$$\nabla \times \vec{H} = \vec{J} + \frac{d\vec{D}}{dt} \qquad (1.2)$$

$$\nabla \cdot \vec{D} = \rho \qquad (1.3)$$

$$\nabla \cdot \vec{B} = 0 \qquad (1.4)$$

Where the above quantities are defined as follows:

$\vec{E}$ the electric field intensity, in V/m;

$\vec{D}$ the electric displacement vector, in Coul/m^2;

$\vec{H}$ the magnetic field intensity, in A/m;

$\vec{B}$ the magnetic displacement vector, in Wb/m^2;

$\vec{J}$ the electric current density, in A/m^2;

ρ the electric charge density, in Coul/m^3 .

These equations are usually combined with the following constitutive relations,

$$\vec{D} = \varepsilon \vec{E} \qquad (1.5)$$

$$\vec{B} = \mu \vec{H} \qquad (1.6)$$

where ε and μ are the dielectric constant and magnetic permeability of the medium respectively, and we have assumed homogeneous, linear and isotropic media. In vacuum ε and μ are denoted as ε_0 and μ_0, which are scalar constants.

Taking the curl of both sides of Eq. (1.1), combining with Eq. (1.2), (1.5), and (1.6), and using the vector triple identity $\nabla \times \nabla \times \vec{E} = \nabla(\nabla \cdot \vec{E}) - \nabla^2 \vec{E}$, we can obtain wave equation,

$$\nabla^2 \vec{E}(r) + k_0^2 n^2(r) \vec{E}(r) = 0 \qquad (1.7)$$

where $k_0^2 \equiv \omega^2 \mu \varepsilon_0 = (2\pi / \lambda)^2$ and $n = \sqrt{\varepsilon / \varepsilon_0}$ is the index of refraction. The solutions are subject to the continuity of the tangential components of $\vec{E}$ and $\vec{H}$ at the dielectric interfaces. In Eq. (1.7) the form of the field is taken as

$$E(r,t) = E(x,y)e^{i(\omega t - \beta z)} \qquad (1.8)$$

β is defined as the propagation constant, which is the z component of the local propagation vector, and a more intuitive quantity to work with is the effective index, N, which is defined as $\beta \equiv Nk_0$ .So that (1.7) becomes

$$\left(\frac{\partial^2}{\partial x^2}+\frac{\partial^2}{\partial y^2}\right)E(x,y)+[k_0^2 n^2(r)-\beta^2]E(x,y)=0 \quad (1.9)$$

The basic features of the behavior of dielectric waveguides can be elucidated with the help of a slab (planar) model in which no variation exists in one (for example, y) dimension. [5] Channel waveguides, in which the waveguide dimensions are finite in both the x and y directions, approach the behavior of the planar guide when one dimension is considerably larger than the other. Even when this is not the case, most of the phenomena of interest are only modified in a simple quantitative way when going from a planar to a channel waveguide. Because of the immense mathematical simplification that results, we will limit most of the following treatment to planar waveguides such as the one shown in the figure 1-1, in which n1, n2, and n3 are the refractive index of cladding layer, core layer and substrate layer respectively. Putting $\partial / \partial y = 0$ in (1.9) and writing it separately in regions I, II, and III yields

Region I $$\frac{\partial^2}{\partial x^2}E(x)+(k_0^2 n_1^2-\beta^2)E(x)=0 \quad (1.10a)$$

Region II $$\frac{\partial^2}{\partial x^2}E(x)+(k_0^2 n_2^2-\beta^2)E(x)=0 \quad (1.10b)$$

Region III $$\frac{\partial^2}{\partial x^2}E(x)+(k_0^2 n_3^2-\beta^2)E(x)=0 \quad (1.10c)$$

where E(x) is the electrical field at the cross section of slab waveguide . In order to obtain stable electrical field solution propagating along z direction without radiating, which is defined as guided mode in Region II, we should specify $k_0 n_3 < \beta < k_0 n_2$, $n_2 > n_1, n_3$,which means the inner layer possesses the highest index of refraction. Thus, the solution is sinusoidal in region II, but is exponential in regions I and III.

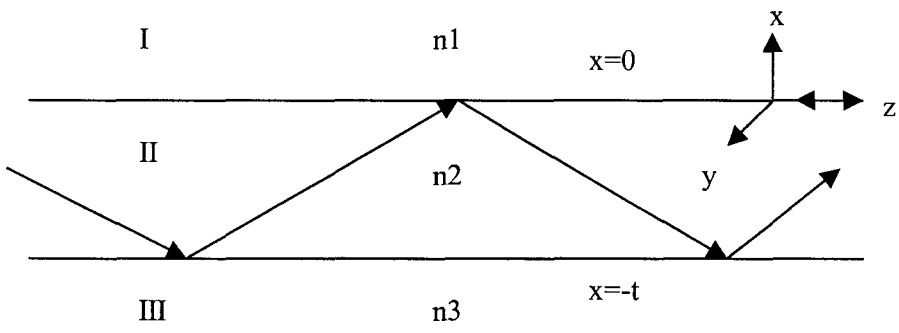

Figure 1-1 A Slab ($\partial / \partial y = 0$) Dielectric Waveguide

Two such solutions are shown in Figure 1-2(b) and (c). The energy carried by these modes is confined to the vicinity of the guiding layer II.

As we consider the propagation constant β in the propagation regime $k_0 n_3 < \beta < k_0 n_2$, the allowed values β are discrete. The number of confined modes depends on the width t, the frequency, and the indices of refraction n_1, n_2, n_3. At a given wavelength the number of confined modes increases from 0 with increasing t. At some t, the mode TE_1 becomes confined. Further increases in t will allow TE_2 to exist as well, and so on. Other situations are considered as radiation modes, like Figure 1-2(d), for which $k_0 n_1 < \beta < k_0 n_3$, and exponential behavior in region I, sinusoidal behavior in regions II and III. For $0 < \beta < k_0 n_1$, as in Figure 1-2 (e), solution becomes sinusoidal in all three regions, and will quickly radiate into free space. Figure 1-2 (a) is just a solution for Eq (1.10), so it is not physically realizable and thus does not correspond to a real wave.

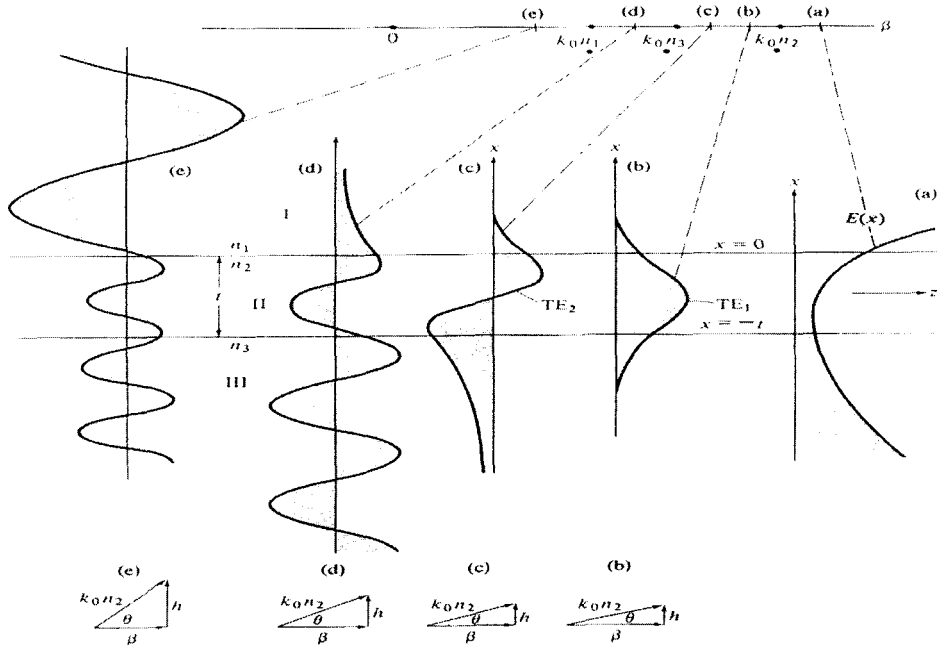

Figure 1-2 The Field Distributions of Different Modes; Different Propagation Constants β.

1.4 TE and TM Modes in an Asymmetric Slab Waveguide [5]

Since this thesis deals with asymmetric ($n_1 \neq n_3$) slab waveguide, it is useful to derive the mode solution for the general asymmetric slab waveguide shown in Figure 1-1. We limit the derivation to the guided modes that according to Figure 1-2 have propagation constants β

$$k_0 n_3 < \beta < k_0 n_2$$

where, to be specific, $n_3 > n_2$.

TE Mode

The field component E_y of the TE modes obeys the wave equation

$$\nabla^2 E_{yi}(x,y,z) + \omega^2 \mu \varepsilon_0 n_i^2 E_{yi} = 0 \qquad \text{i=1, 2, 3} \quad (1.11\text{-}1)$$

where Region I refers to the layer and the (real) electric field is given by

$$E_{yi}(x,y,z,t) = \mathrm{Re}[E_{yi}(x,y,z)e^{i\omega t}]$$

For waves propagating along the z direction and for $\partial/\partial y = 0$ we have

$$E_{yi}(x,y,z) = E_y(x)e^{-i\beta z} \qquad (1.11\text{-}2)$$

The transverse function $E_{yi}(x)$ is taken as

$$E_y = \begin{cases} C\exp(-qx) & 0 \le x < \infty \\ C(\cos xh - \frac{q}{h}\sin xh) & -t \le x \le 0 \\ C(\cos th + \frac{q}{h}\sin th)\exp[p(x+t)] & -\infty < x \le -t \end{cases} \qquad (1.11\text{-}3)$$

Applying (1.11-1) to (1.11-3) results in

$$\begin{aligned} h &= (n_2^2 k_0^2 - \beta^2)^{1/2} \\ q &= (\beta^2 - n_1^2 k_0^2)^{1/2} \\ p &= (\beta^2 - n_3^2 k_0^2)^{1/2} \\ k_0 &\equiv \frac{\omega}{c} \end{aligned} \qquad (1.11\text{-}4)$$

The acceptable solutions for E_y and $H_z = (i/\omega\mu)(\partial E_y/\partial x)$ should be continuous at both x=0 and x=-t. The choice of coefficients in (1.11-3) is such as to make E_y continuous at both interfaces as well as $(\partial E_y/\partial x)$ at x=0. By imposing the continuity requirement on $\partial E_y/\partial x$ at x=-t, we get from (1.11-3)

$$h\sin th - q\cos th = p(\cos th + \frac{q}{h}\sin th) \qquad (1.11\text{-}5)$$

The constant, C, appearing in (1.11-3) is arbitrary, yet for many applications, especially those in which propagation and exchange of power involve more than one mode, it is advantageous to define C in such a way that it is simply related to total power in the mode. We choose C so that the field $E_y(x)$ in (1.11-3) corresponds to a power flow of one watt (per unit width in y direction) in the mode. A mode for which $E_y=AE_y(x)$ will thus correspond to a power flow of $|A|^2$ watts/m. The normalization condition becomes

$$-\frac{1}{2}\int_{-\infty}^{\infty} E_y H_x^* dx = \frac{\beta_m}{2\omega\mu}\int_{-\infty}^{\infty}\left[E_y^{(m)}(x)\right]^2 dx = 1 \qquad (1.11\text{-}6)$$

where the symbol m denotes the *m*th confined TE mode and $H_x = -i(\omega\mu)^{-1}\partial E_y/\partial z$.

Using (1.11-3) in (1.11-6) leads, after substantial but straightforward calculation, to

$$C_m = 2h_m\left(\frac{\omega\mu}{|\beta_m|[t+(1/q_m)+(1/p_m)](h_m^2+q_m^2)}\right)^{1/2} \qquad (1.11\text{-}7)$$

Since the modes $E_y^{(m)}$ are orthogonal, we have

$$\int_{-\infty}^{\infty} E_y^{(l)} E_y^{(m)} dx = \frac{2\omega\mu}{\beta_m}\delta_{l,m} \qquad (1.11\text{-}8)$$

TM Modes

The derivation of the confined TM modes is similar in principle to that of the TE modes. The field components are

$$H_y(x,z,t) = H_y(x)e^{i(\omega t-i\beta z)}$$

$$E_x(x,z,t) = \frac{i}{\omega\varepsilon}\frac{\partial H_y}{\partial z} = \frac{\beta}{\omega\varepsilon}H_y(x)e^{i(\omega t-\beta z)} \qquad (1.11\text{-}9)$$

$$E_z(x,z,t) = -\frac{i}{\omega\varepsilon}\frac{\partial H_y}{\partial x}$$

The transverse function, $H_y(x)$, is taken as

$$H_y(x) = \begin{cases} -C(\frac{h}{\bar{q}}\cos th + \sin th)e^{p(x+t)} & x \le -t \\ C(-\frac{h}{\bar{q}}\cos xh + \sin xh) & -t \le x \le 0 \\ -\frac{h}{\bar{q}}Ce^{-qx} & x \ge 0 \end{cases} \qquad (1.11\text{-}10)$$

The continuity of H_y and E_z at the two interfaces leads, in a manner similar to (1.11-5), to the eigenvalue equation

$$\tan th = \frac{h(\bar{p}+\bar{q})}{h^2 - \bar{p}\bar{q}} \qquad (1.11\text{-}11)$$

where

$$\bar{p} \equiv \frac{n_2^2}{n_3^2}p \qquad \bar{q} = \frac{n_2^2}{n_1^2}q$$

The normalization constant, C, is chosen so that the field represented by (1.11-9) and (1.11-10) carries one watt per unit width in the y direction

$$\frac{1}{2}\int_{-\infty}^{\infty} H_y E_x^* dx = \frac{\beta}{2\omega}\int_{-\infty}^{\infty}\frac{H_y^2(x)}{\varepsilon(x)}dx = 1$$

Carrying out the integration using (1.11-10) gives

$$C_m = 2\sqrt{\frac{\omega\varepsilon_0}{\beta_m t_{eff}}}$$

$$t_{eff} \equiv \frac{\bar{q}^2 + h^2}{\bar{q}^2}\left(\frac{t}{n_2^2} + \frac{q^2 + h^2}{\bar{q}^2 + h^2}\frac{1}{n_1^2 q} + \frac{p^2 + h^2}{\bar{p}^2 + h^2}\frac{1}{n_3^2 p}\right) \qquad (1.11\text{-}13)$$

Normalized frequency V and the normalized guide index b are defined as

$$V = k_0 t\sqrt{n_2^2 - n_3^2} \qquad (1.12)$$

and

$$b = (N^2 - n_3^2)/(n_2^2 - n_3^2) \qquad (1.13)$$

$$a_{TE} = (n_3^2 - n_1^2)/(n_2^2 - n_3^2) \qquad (1.14) \text{ for TE modes}$$

$$a_{TM} = \left(\frac{n_2}{n_1}\right)^2 \frac{n_3 - n_1}{n_2 - n_3} \qquad (1.15) \text{ for TM modes}$$

in asymmetry waveguides. Using definitions (1.12) to (1.15), the eigenvalue equation (1.11-5) can be rewritten in the normalized form

$$V\sqrt{1-b} = (m+1)\pi + \tan^{-1}\sqrt{b/(1-b)} + \tan^{-1}\sqrt{(b+a)/(1-b)} \qquad (1.16)$$

where m=0, 1, 2, 3... denotes the mode number. A numerical evaluation for the above expression yields a normalized dispersion curve as presented in Figure 1-3. [6] In general a mode becomes confined above a certain (cutoff) value of t/λ. At the cutoff value p=0, and the mode extends to $x=-\infty$. For increasing values of t/λ, p>0, and the mode becomes increasingly confined to layer 2. This is reflected in the effective mode index $\beta\lambda/2\pi$ that, at cutoff, is equal to n_3, and which, for large t/λ, approaches n_2.

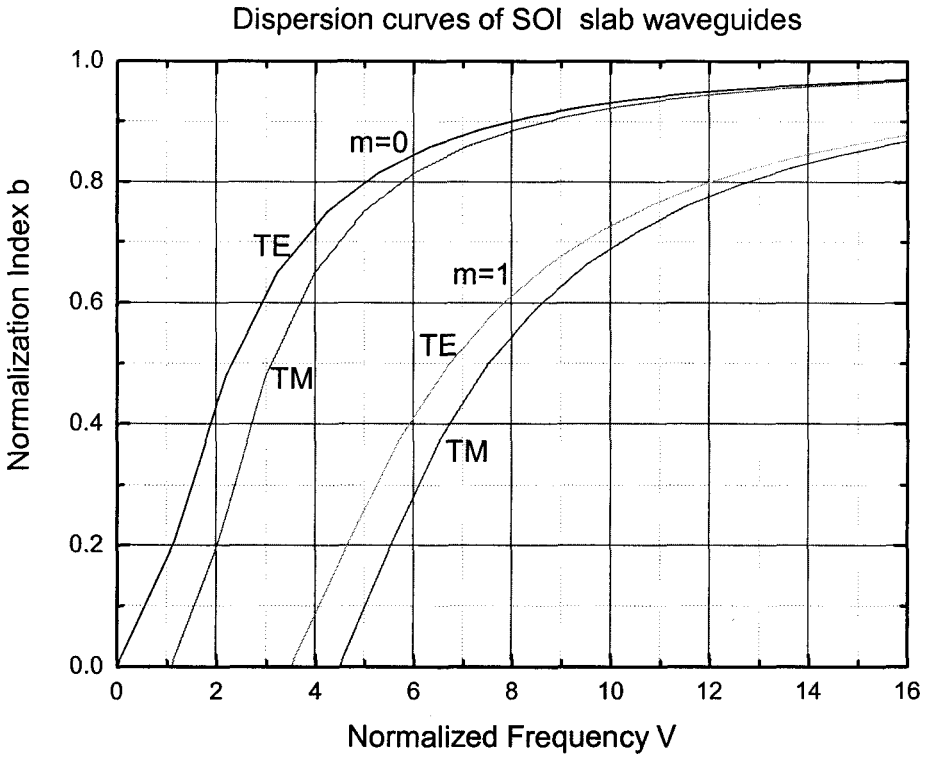

Figure 1-3 Dispersion Curves for the Fundamental Mode of Silicon on Insulator Waveguides, n1=1, n2=3.5, n3=1.45

CHAPTER 2 SOI OPTICAL WAVEGUIDES

2.1 Introduction to Silicon-On-Insulator (SOI)

Silicon-on-insulator (SOI) is a critical material for future photonic-integrated circuits (PIC). The SOI structure possesses unique optical properties owing to the large refractive index difference between silicon (n=3.5) and SiO_2 (n=1.45). This has led to the investigation of the optical properties of SOI waveguides and the development of a number of photonic integrated circuits (PIC's). Excellent optical properties as well as true compatibility with silicon CMOS integrated circuit technology are highly promising for future low-cost photonic integrated circuits. [7]

In my research, the SOI wafers are purchased from IBIS Technology Inc. These SOI wafers are fabricated by SIMOX technology [8] [22], which means Separation by Implanted Oxygen technology uses implantation of oxygen at high doses (~10^{18} cm^{-3}) followed by a high temperature anneal to form a buried SiO_2 layer in a silicon wafer. Figure 2-1 is the basic configuration of SOI structure. In this thesis, the SOI wafers that were used had layer thickness of: 2.2um/1.09um/675um for $Si/SiO_2/Si$ respectively. I used 2.2um SOI because, in thin top silicon layer, gratings will compose strong perturbation of transmission waves.

Single mode propagation with low loss is a prerequisite for the operation of most PIC's. Conventional wisdom suggests that the large refractive index step in SOI prevents single mode propagation unless the waveguide has submicrometer transverse dimensions, in which case it will have extremely poor coupling efficiency to optical fibers. However, as shown by Soref and Pogossian [9] [10], single mode propagation is possible in SOI waveguides with transverse dimensions that are large compared to the optical wavelength in the material. They proposed a simple relation, equation (2.1)

between the width and the etch depth of rib waveguides for the single mode propagation.

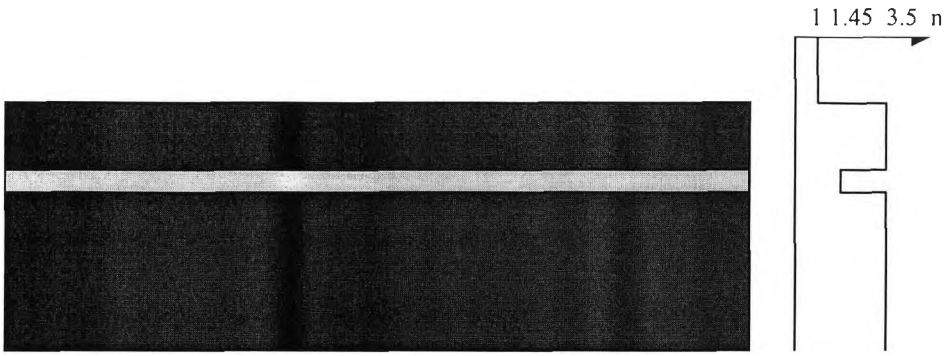

Figure 2-1 Silicon-on-Insulator (SOI) Structure

$$t < r/(1-r^2)^{1/2} \qquad (2.1)$$

where $t = w_{eff}/H_{eff}$, $r = h_{eff}/H_{eff}$, $h_{eff} = h+q$, $H_{eff} = H+q$,

$q = \gamma_c/\{k(n_f^2-n_c^2)^{1/2}\} + \gamma_s/\{k(n_f^2-n_s^2)^{1/2}\}$,

$w_{eff} = w + 2\gamma_c/\{k(n_f^2-n_c^2)^{1/2}\}$, n_f, n_s, and n_c are refractive indices of the guiding region, the substrate and the air respectively as shown in Figure 2-2.

$\gamma_{c,s} = 1$ for TE modes and $(n_{c,s}/n_f)^2$ for TM modes, $k=2\pi/\lambda$, λ is the wavelength.

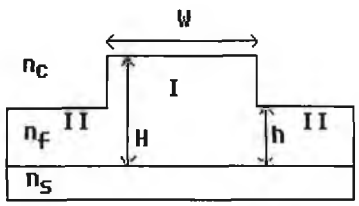

Figure 2-2 SOI Rib Waveguide Structure

This interesting phenomenon occurs in rib waveguide. While the rib waveguide may be multimode, the higher order modes "leak" into the surrounding slab regions during propagation resulting in an effective single mode propagation in the rib region [11], which will be illustrated in beam propagation method in the next section.

2.2 Modeling Methods

There are many different methods to simulate and analyze integrated optic devices. This thesis uses primarily the effective index method (EIM) and the beam propagation method (BPM). The EIM is usually used for calculating the propagation constants of the guided modes, and BPM is used to simulate the transmission of light through a photonic device.

2.2.1 The Effective Index Method [12]

The effective index method is a useful technique to find the propagation constant of a dielectric waveguide. As an example, a waveguide structure such as illustrated in Figure 2-2(a) can be separated into three different regions as Figure 2-2(b). We first solve a slab waveguide problem with refractive index n_f inside and n_c, n_s out side the waveguide. The eigenequation for the E_y component will be that of the TE modes of a slab guide. We can use (1.12) to calculate the normalized frequency, in which t is the thickness H or l of each region respectively.

Combining (1.12) to (1.14) these parameters into the eigenvalue equation for the TE modes, we can obtain

$$V\sqrt{1-b} = (m+1)\pi + \tan^{-1}\sqrt{\frac{b}{1-b}} + \tan^{-1}\sqrt{\frac{b+a}{1-b}} \qquad (1.16)$$

where m=0,1,2,....This can be used to solve the effective indices N_f and N_l. When the effective index in each region is determined, we can determine the effective index of the rib waveguide by calculating the three layers slab waveguide horizontally with the waveguide width **W**, as Figure 2-3 (c).

(a) The cross section of ridge waveguide

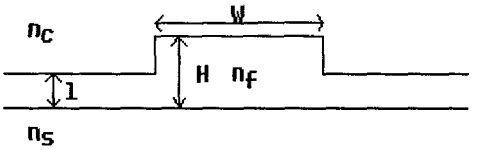

(b) Slab waveguide in the vertical direction

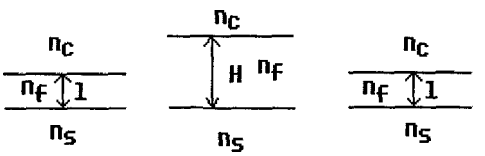

(c) Slab waveguide in lateral direction

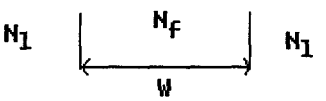

Figure 2-3 Cross Section of a Rib Waveguide Used With the EIM

This method can be easily used by computer algorithms. In my research, MATLAB programs are used to calculate the effective index of the fundamental mode of a rib SOI waveguide. I use 4um wide SOI rib and an etch depth of 0.2 um. From the Table 2-1, we can see all the higher order modes in the central region have effective index smaller than the effective index of the lowest order mode in the side regions, which means these higher order modes will not satisfy the total internal reflection, and will quickly radiate into side region. By restricting the ribs etch depth to values for which this condition is met, we can achieve single mode operation of rib SOI waveguides.

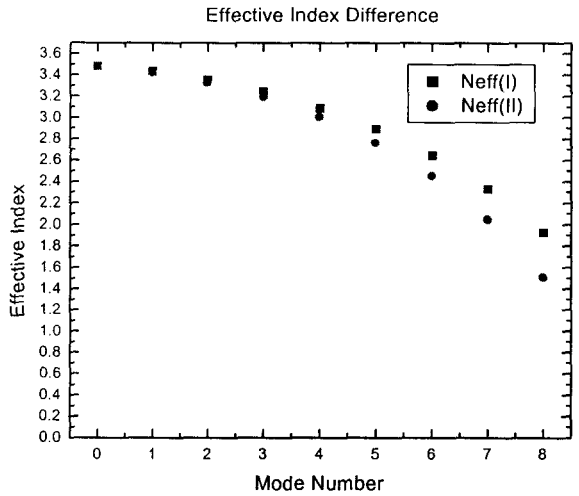

	Neff(I)	Neff(II)
Mode 0	3.48444483	3.48141087
Mode 1	3.43739931	3.42510469
Mode 2	3.35767571	3.32938451
Mode 3	3.24312131	3.19112431
Mode 4	3.09029987	3.00520005
Mode 5	2.89389156	2.76335332
Mode 6	2.64553219	2.45181231
Mode 7	2.33141092	2.04596846
Mode 8	1.92708015	1.50807675

Neff (I): Mode N_{eff} in Central Region

Neff (II): Mode N_{eff} in Side Region

Table 2-1 Effective Index Difference in Rib SOI Central (2.2um) and Side (2um) Regions

However, if the rib etch depth is as deep as 1um, mode 1 in the central region will have larger effective index than the fundamental mode in the side region, which means mode 1 will also be confined in the central region resulting in multimode operation. Since the side region is etched down to 1.2um thick, there are only 4 modes supported and other higher order modes will be cutoff. Table 2-2 presents this case as an opposite example comparing to Table 2-1.

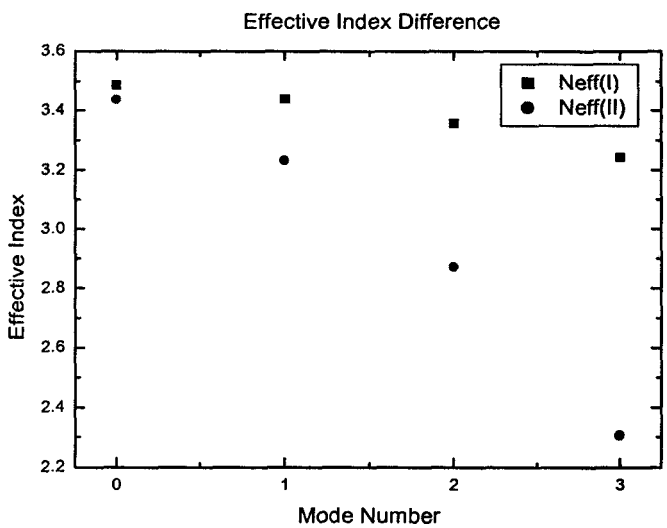

	Neff(I)	Neff(II)
Mode 0	3.48444483	3.43481231
Mode 1	3.43739931	3.23308878
Mode 2	3.35774947	2.87316582
Mode 3	3.24326245	2.30447149

Neff (I): Mode N_{eff} in Central Region

Neff (II): Mode N_{eff} in Side Region

Table 2-2 Effective Index Difference in Rib SOI Central (2.2um) and Side (1.2um) Regions

2.2.2 The Beam Propagation Method

The BPM method is simple in implementation and extremely versatile. It allows simulation of the electric field as light travels through a waveguide structure, and includes higher order and radiation mode effects. The basic idea of BPM is propagating an input light beam over a very small distance through homogeneous media and correcting the index profile changes (i.e. geometry changes) in the propagation direction, during this distance to simulate mode propagation.

I use Optiwave BPM [13] [14] and Apollo Photonics [15] software to simulate the single mode condition of rib SOI waveguide. Figure 2-4 and 2-5 are the computer simulation pictures of fundamental mode profile in the rib waveguides, and 3 dimensional image of fundamental mode which demonstrate the mode intensity distribution. We find the 4 um wide, 0.2um deep rib SOI waveguide is truly single mode as shown in Figure 2-6. Figure 2-7 is the CCD camera photo of single mode image, from this photo we can observe that only one bright light spot in the whole image which is the experimental proof of single mode operation.

Furthermore, if we intentionally couple higher order modes as presented in Figure 2-8 into this kind of structure, all the higher order modes will quickly leak away into the side region, which is illustrated in Figure 2-9.

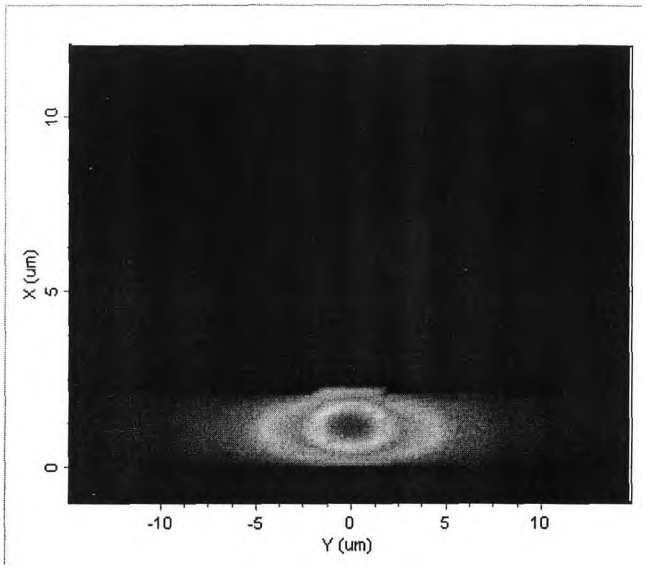

Figure 2-4 Side View of Single Mode Profile

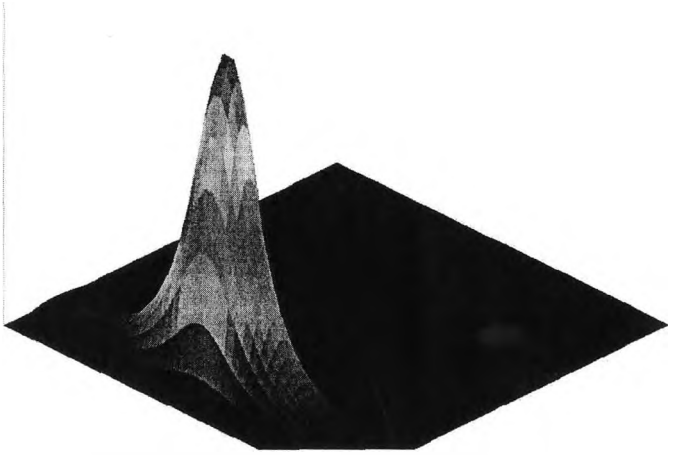

Figure 2-5 Three Dimentional View of Single Mode Profile

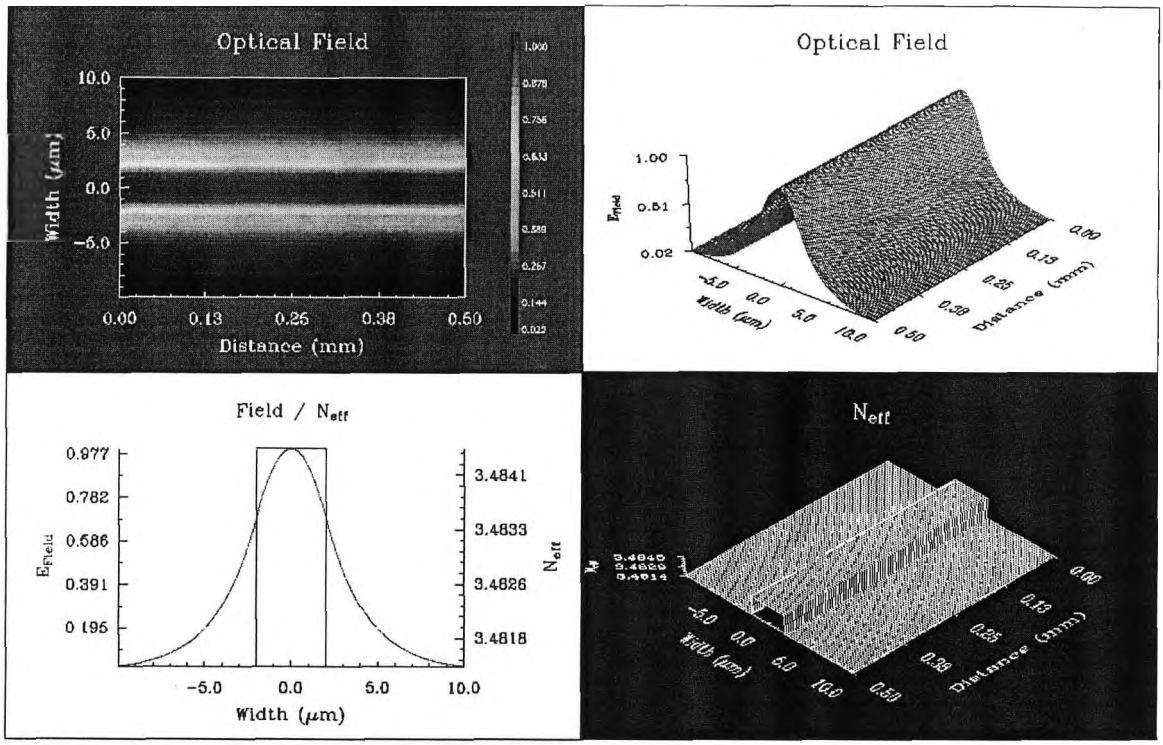

Figure 2-6 Single Mode Characteristics of SOI Waveguides

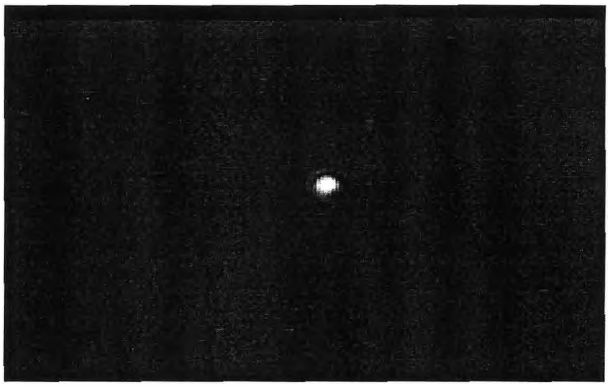

Figure 2-7 Single Mode Profile from IR CCD Camera

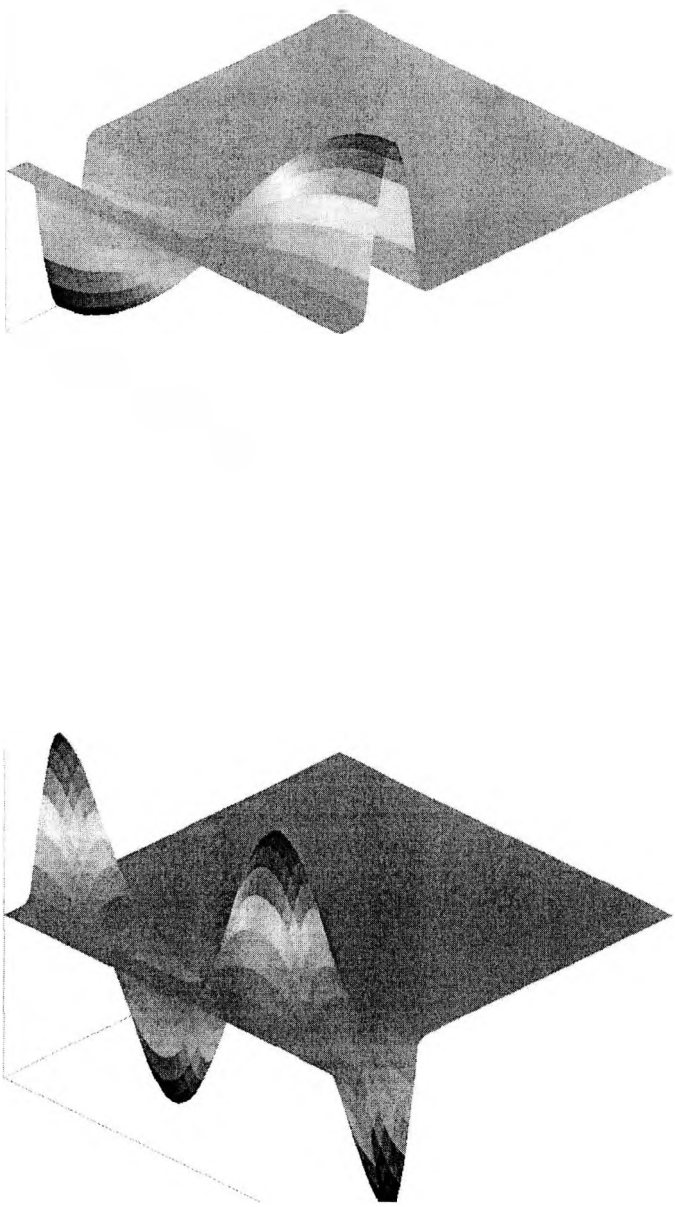

Figure 2-8 Higher Order Mode Profiles

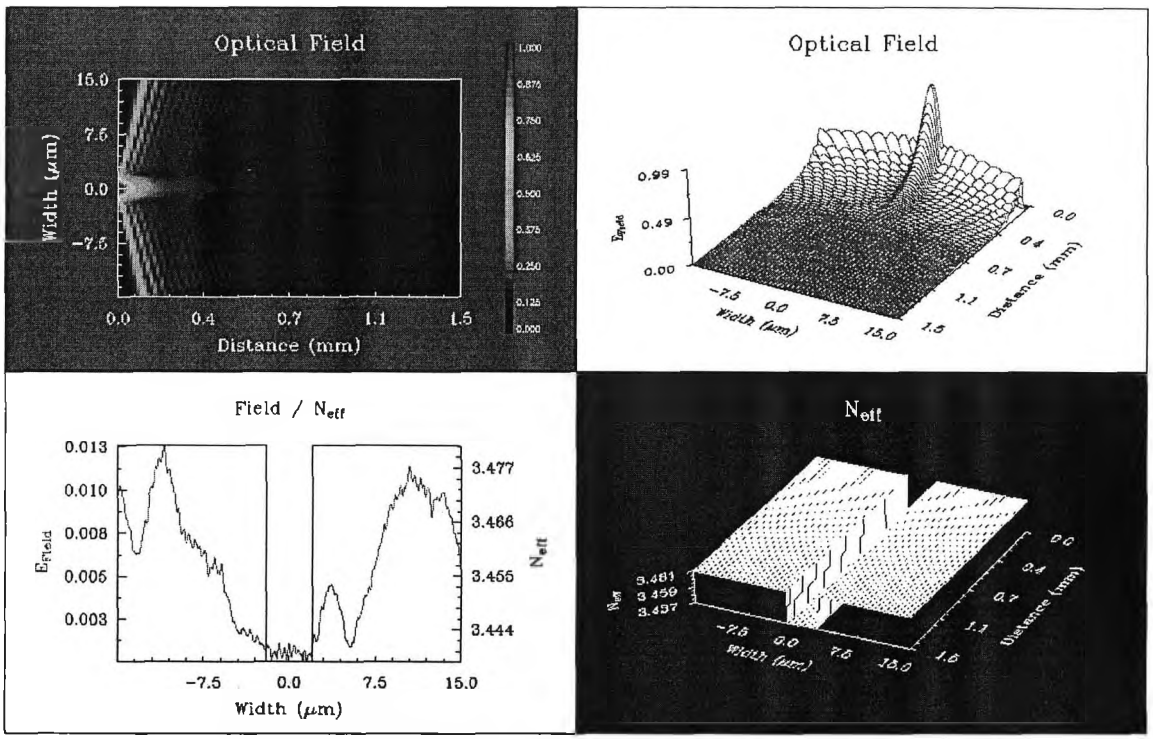

Figure 2-9 Leaky Mode Characteristics of SOI Waveguides

CHAPTER 3 Theories and Analysis

3.1 Bragg Grating Basics

The Bragg grating may be though of as a one dimensional diffraction grating which diffracts light from the forward traveling mode into the backward traveling mode. The condition for diffraction into the reverse traveling mode is called the Bragg condition. In order for light to be efficiently diffracted in the opposite direction, the reflections from subsequent periods of the grating must interfere constructively. The principle of reflection from a Bragg grating in a waveguide structure is illustrated schematically in Figure 3-1. This means that the Bragg period Λ must be related to the free space wavelength λ_0 by:

$$\Lambda = \frac{\lambda_0}{2N} \qquad (3.1)$$

where N is the effective index of refraction of the structure, which depends on the materials comprising the waveguide. λ_0 / N is the wavelength inside of the dielectric material. Because the period of the grating is precisely half of the wavelength of light in the waveguide, the reflections from subsequent teeth in the grating generate constructive interference.

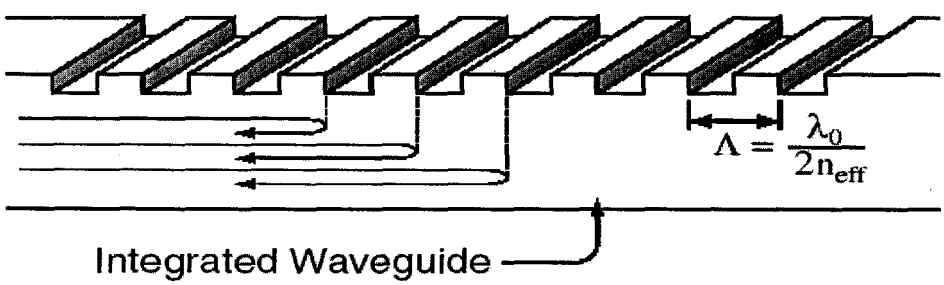

Figure 3-1 Schematic Illustration of Bragg Reflection

Generally speaking, for fiber optic networks the desired operating wavelength is approximately 1550 nm. Table 3-1 lists the appropriate Bragg grating periods for a few common waveguide materials.

Eq (3.1) assumes that the phase accumulation between reflections from adjacent grating teeth is precisely half wavelength. This is the condition for a first order Bragg grating. It is also possible to utilize higher order diffraction to couple to the forward and backward modes. The more general condition for constructive interference is that the phase accumulation between subsequent reflections must be an integral number of wavelengths. The Bragg condition for an L^{th} order Bragg grating is:

$$\Lambda = \frac{L\lambda_0}{2N} \qquad (3.2)$$

In this work, we consider only first-order (L=1) Bragg gratings, because the diffraction efficiency which means the contradirectional coupling strength is generally strongest for the first diffracted order. Nevertheless, some people build higher order Bragg gratings simply because the required grating pitch is substantially larger, which simplifies the fabrication process.

Material	Si	InP/InGaAsP	SiO2
n (refractive index)	3.5	3.17	1.46
Bragg grating period	220nm	245nm	535nm

Table 3-1 Bragg Periods Λ for Some Common Waveguide Materials, Assuming a Free Space Operating Wavelength of 1550nm

3.2 A Perturbation Theory of Coupled Modes in Dielectric Optical Waveguides [5] [16] [17]

In chapter 2, we obtained solutions for the confined modes supported by a slab dielectric waveguide. An increasingly large number of experiments and devices involve coupling between such modes. A typical example is coupling of forward-to-backward modes by means of a corrugation in one of the waveguide interface. In this segment, such coupling will be described.

We start with the wave equation in the form

$$\nabla^2 E(r,t) = \mu\varepsilon_0 \frac{\partial^2 E(r,t)}{\partial t^2} + \mu \frac{\partial^2}{\partial t^2} P(r,t) \qquad (3.3)$$

The total medium polarization can be taken as the sum

$$P(r,t) = P_0(r,t) + P_{pert}(r,t) \qquad (3.4)$$

where $$P_0(r,t) = [\varepsilon(r) - \varepsilon_0]E(r,t) \qquad (3.5)$$

is the polarization induced by E(r, t) in the unperturbed waveguide whose dielectric constant is ε(r). The perturbation polarization P_{pert}(r, t) is then defined by (3.4) and represents any deviation of the polarization from that of the unperturbed waveguide. Using (3.4) and (3.5) in (3.3) gives

$$\nabla^2 E_y - \mu\varepsilon(r) \frac{\partial^2 E_y}{\partial t^2} = \mu \frac{\partial^2}{\partial t^2} [P_{pert}(r,t)]_y \qquad (3.6)$$

and similar expressions for E_x and E_z.

Ignoring the possibility of coupling to the continuum of radiation modes, we expand the total field in the "perturbed" waveguide as a superposition of confined modes

$$E_y(r,t) = \frac{1}{2} \sum_m A_m(z) E_y^{(m)}(x) e^{i(\omega t - \beta_m z)} + c.c. \qquad (3.7)$$

where m indicates the *m*th discrete eigenmode which satisfies

$$(\frac{\partial^2}{\partial x^2} - \beta_m^2)E_y^{(m)}(x) + \omega^2\mu\varepsilon(r)E_y^{(m)}(x) = 0 \qquad (3.8)$$

where $\varepsilon(r) = \varepsilon_0 n^2(r)$.

Substitution of (3.7) in (3.6) leads to

$$e^{i\omega t}\sum_m [\frac{A_m}{2}(-\beta_m^2 E_y^{(m)} + \frac{\partial^2 E_y^{(m)}}{\partial x^2} + \omega^2\mu\varepsilon(r)E_y^{(m)})e^{-i\beta_m z} + \frac{1}{2}(-2i\beta_m\frac{dA_m}{dz} + \frac{d^2A_m}{dz^2})E_y^{(m)}e^{-i\beta_m z}] + c.c$$

$$= \mu\frac{\partial^2}{\partial t^2}[P_{pert}(r,t)]_y \qquad (3.9)$$

And we not that in view of (3.8) the sum of the first three terms in (3.9) is zero. We assume "slow" variation so that

$$\left|\frac{d^2A_m}{dz^2}\right| << \beta_m\left|\frac{dA_m}{dz}\right|$$

and obtain from (3.9)

$$\sum_m -i\beta_m\frac{dA_m}{dz}E_y^{(m)}e^{i(\omega t-\beta_m z)} + c.c. = \mu\frac{\partial^2}{\partial t^2}[P_{pert}(r,t)]_y \qquad (3.10)$$

And take the product of (3.10) with $E_y^{(s)}(x)$ and integrate from - to . The result, using (1.11-10), is

$$\frac{dA_s^{(-)}}{dz}e^{i(\omega t+\beta_s z)} - \frac{dA_s^{(+)}}{dz}e^{i(\omega t-\beta_s z)} - c.c.$$

$$= -\frac{i}{2\omega}\frac{\partial^2}{\partial t^2}\int_{-\infty}^{\infty}[P_{pert}(r,t)]_y E_y^{(s)}(x)dx \qquad (3.11)$$

The presence of two terms on the left side of (3.11) is due to the fact that the summation over m in (3.10) contains two terms involving $E_y^{(m)}(x)$ for each value of m, one wave designated as (-), traveling in the –z direction, and the other (+), traveling in the +z direction.

Equation (3.11) can be used to treat a large variety of mode interactions, and in my experiment, I am most concerned with periodic waveguides.

3.3 Periodic Waveguide

Consider a periodic dielectric waveguide in which the periodicity is due to a corrugation of one of the interfaces as shown in Figure 3-1. Such periodic waveguides are used for optical filtering.

The Corrugation is described by the dielectric perturbation $\Delta\varepsilon(r) \equiv \varepsilon_0 \Delta n^2(r)$ such that the total dielectric constant is

$$\varepsilon'(r) = \varepsilon(r) + \Delta\varepsilon(r)$$

The perturbation polarization is from (3.2) and (3.3)

$$P_{pert}(r,t) = \Delta\varepsilon(r)E(r,t) = \Delta n^2(r)\varepsilon_0 E(r,t) \qquad (3.12)$$

Since $\Delta n^2(r)$ is a scalar, it follows from (3.6) that the corrugation couples only TE to TE modes and TM to TM, but not TE to TM.

To be specific, consider TE mode propagation. Using (3.7) in (3.12) gives

$$[P_{pert}(r,t)]_y = \frac{\Delta n^2(r)\varepsilon_0}{2}\sum_m [A_m E_y^{(m)}(x)e^{i(\omega t-\beta_m z)} + c.c.] \qquad (3.13)$$

which, when used in (1.11-9), leads to

$$\frac{dA_s^{(-)}}{dz}e^{i(\omega t+\beta_s z)} - \frac{dA_s^{(+)}}{dz}e^{i(\omega t-\beta_s z)} - c.c.$$

$$= -\frac{i\varepsilon_0}{4\omega}\frac{\partial^2}{\partial t^2}\sum_m [A_m \int_{-\infty}^{\infty} \Delta n^2(x,z) E_y^{(m)}(x) dx e^{i(\omega t - \beta_m z)} + c.c] \qquad (3.14)$$

The right side of (3.14) may be considered as a source wave term driving the forward wave $A_s^{(+)} \exp[i(\omega t - \beta_s z)]$ and the backward wave $A_s^{(-)} \exp[i(\omega t + \beta_s z)]$ on the left side. In order for a wave to be driven by a source, both source wave and driven wave must have the same frequency so that the interaction will not average out to zero over a long time (long compared to a period of their difference frequency). Equally important: Both source and driven wave need to have nearly the same phase dependence exp (iβz) so that the interaction does not average out to zero with distance of propagation z. If, for example, it is desired that the forward wave $A_s^{(+)}\exp[i(\omega t-\beta z)]$ be excited, it is necessary that at least one term on the right side of (3.14), say the *l*th one, vary as exp[i(ωt-βz)] with $\beta \approx \beta_s$. If no other terms on the right side of (3.14) satisfy this condition, we simplify the equation by keeping only the forward wave on the left side and *l*th on the right. We describe this situation by saying that the perturbation $\Delta n^2(x, z)$ couples the forward (+s) mode to the *l*th mode and vice versa.

To be specific, let us assume that the period Λ n the z direction of the perturbation $\Delta n^2(x,z)$ is so chosen that $l\pi/\Lambda \approx \beta_s$ for some integer l. We can expand $\Delta n^2(x, z)$ of a square wave perturbation as a Fourier series

$$\Delta n^2(x,z) = \Delta n^2(x) \sum_{q=-\infty}^{\infty} a_q e^{i(2q\pi/\Lambda)z} \qquad (3.15)$$

The right side of (3.14) now contains a term (q=l, m=s) proportional to $A_s^{(+)}\exp[i(2l\pi/\Lambda-\beta_s)z]$. But $\frac{2l\pi}{\Lambda} - \beta_s \approx \beta_s$, so that this term is capable of driving synchronously the amplitude $A_s^{(-)}\exp(i\beta_s z)$ on the left side of (3.14) with the result

$$\frac{dA_s^{(-)}}{dz} = \frac{i\omega\varepsilon_0}{4} A_s^{(+)} \int_{-\infty}^{\infty} \Delta n^2(x)[E_y^{(s)}(x)]^2 dx a_l e^{i[(2l\pi/\Lambda)-2\beta_s]z} \qquad (3.16)$$

The coupling between the backward $A_s^{(-)}$ and the forward $A_s^{(+)}$ by the *l*th harmonic of $\Delta n^2(x,z)$ can thus be described by

$$\frac{dA_s^{(-)}}{dz} = \kappa A_s^{(+)} e^{-i2(\Delta\beta)z} \qquad (3.17)$$

and reciprocally

$$\frac{dA_s^{(+)}}{dz} = \kappa^* A_s^{(-)} e^{i2(\Delta\beta)z}$$

where

$$\kappa = \frac{i\omega\varepsilon_0 a_l}{4} \int_{-\infty}^{\infty} \Delta n^2(x)[E_y^{(s)}(x)]^2 dx \qquad (3.18)$$

$$\Delta\beta \equiv \beta_s - \frac{l\pi}{\Lambda} \equiv \beta_s - \beta_0 \qquad (3.19)$$

We note that the total power carried by both modes is conserved, since

$$\frac{d}{dz}[|A_s^{(-)}|^2 - |A_s^{(+)}|^2] = 0 \qquad (3.20)$$

Let us consider the specific "square-wave" corrugation of figure 3-2. In this case the periodicity (period = Λ) in the z direction is accounted for by taking

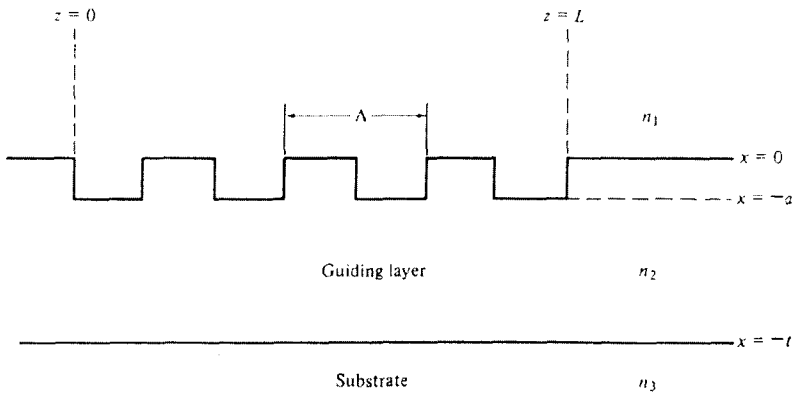

Figure 3-2 A Corrugated Periodic Waveguide

$$\Delta n^2(x,z) = \Delta n^2(x)[\frac{1}{2} + \frac{2}{\pi}(\sin\eta z + \frac{1}{3}\sin 3\eta z + ...)]$$

$$= \Delta n^2(x)\sum_l a_l e^{il\eta z} \qquad \text{l=1, 3, 5...} \qquad (3.21)$$

where

$$\Delta n^2(x) = \begin{cases} n_1^2 - n_2^2 & -a \le x \le 0 \\ 0 & elsewhere \end{cases} \qquad (3.22)$$

$$\eta = \frac{2\pi}{\Lambda}$$

so that

$$a_l = \begin{cases} \dfrac{-i}{\pi l} & l = odd \\ 0 & l = even \\ \dfrac{1}{2} & l = 0 \end{cases}$$

and for l odd we obtain from (3.18) and (3.21)

$$\kappa = \frac{\omega \varepsilon_0}{4\pi l} \int_{-\infty}^{\infty} \Delta n^2(x)[E_y^{(s)}(x)]^2 dx \qquad (3.23)$$

In practice the period Λ is chosen so that, for some particular l, $\Delta\beta \approx 0$. We note that for $\Delta\beta = 0$

$$\Lambda = l\frac{\lambda_g^{(s)}}{2} \qquad (3.24)$$

where $\lambda_g^{(s)} = 2\pi / \beta_s$ is the guide wavelength of the sth mode.

We can now use the field expansion (1.11-3) plus (3.22) to perform the integration of (3.23)

$$\int_{-\infty}^{\infty} \Delta n^2(x)[E_y^{(s)}(x)]^2 dx = (n_1^2 - n_2^2)\int_a^0 [E_y^{(s)}(x)]^2 dx$$

$$= (n_1^2 - n_2^2)C_s^2 \int_a^0 [\cos xh_s - \frac{q_s}{h_s}\sin xh_s]^2 dx \qquad (3.25)$$

Although the integral can be calculated exactly from (1.11-3) and (1.11-5), but an especially simple result follows if we consider that operation is sufficiently above propagation cutoff, $t(n_2-n_3)/s\lambda >> 1$ so that from (1.11-4) and (1.11-5)

$$\beta_s \approx n_2 k_0$$

$$h_s \to \frac{\pi s}{t} \qquad \text{s=1, 2,...= transverse mode number}$$

$$\frac{q_s}{h_s} \approx (n_2^2 - n_1^2)^{1/2}(\frac{2t}{s\lambda}) \qquad (3.26)$$

The results can be verified using (1.11-4) and (1.11-5). In addition since $q_s >> h_s$, we have, from (1.11-7),

$$C_s^2 = \frac{4h_s^2 \omega\mu}{\beta_s t q_s^2} \qquad (3.27)$$

in the well confined regime and has $h_s a << 1$ the integral of (3.25) becomes

$$(n_1^2 - n_2^2)\int_{-a}^{0}[E_y^{(s)}(x)]^2 dx = (n_1^2 - n_2^2)\frac{4\pi^2\omega\mu}{3n_2 k_0}(\frac{a}{t})^3 s^2(1+\frac{3}{q_s a}+\frac{3}{q_s^2 a^2})$$

and, using (3.26)

$$\kappa \approx \frac{2\pi^2 s^2}{3l\lambda}\frac{(n_2^2 - n_1^2)}{n_2}(\frac{a}{t})^3[1+\frac{3}{2\pi}\frac{\lambda/a}{(n_2^2 - n_1^2)^{1/2}}+\frac{3}{4\pi^2}\frac{(\lambda/a)^2}{(n_2^2 - n_1^2)}] \quad (3.28)$$

The problem of two wave coupling by a corrugation has thus been deduced to a pair of coupled differential equations (3.17) and an expression (3.28) for the coupling constant.

3.4 Coupled Mode Solutions

Let us return to the coupled mode equations (3.17). For simplicity let us put $A_s^{(-)} \equiv A$, $A_s^{(+)} \equiv B$ and write them as

$$\frac{dA}{dz} = \kappa_{ab} B e^{-i2(\Delta\beta)z}$$

$$\frac{dB}{dz} = \kappa_{ab}^{*} A e^{+i2(\Delta\beta)z} \quad (3.29)$$

Consider a waveguide with a corrugated section of length L as in Figure 3-2. A wave with an amplitude B(0) is incident from the left on the corrugated section.

The solution of (3.29) for this case subject to A(L)=0 is

$$A(z)e^{i\beta z} = B(0)\frac{ik_{ab}e^{i\beta_0 z}}{-\Delta\beta\sinh(SL)+iS\cosh(SL)}\sinh[S(z-L)] \quad (3.30)$$

$$B(z)e^{-i\beta z} = B(0)\frac{e^{-i\beta_0 z}}{-\Delta\beta h(SL)+iS\cosh(SL)}\cdot\{\Delta\beta\sinh[S(z-L)]+iS\cosh[S(z-L)]\}$$

where

$$S = \sqrt{\kappa^2 - (\Delta\beta)^2}$$

$$\kappa \equiv |\kappa_{ab}| \tag{3.31}$$

Under the phase matching conditions Δβ=0, we have

$$A(z) = B(0)\frac{\kappa_{ab}}{\kappa}\frac{\sinh[\kappa(z-L)]}{\cosh \kappa L}$$

$$B(z) = B(0)\frac{\cosh[\kappa(z-L)]}{\cosh \kappa L} \tag{3.32}$$

A plot of the mode powers $|B(z)|^2$ and $|A(z)|^2$ for this case is shown in Figure 3-3. For sufficiently large arguments of the cosh and sinh function in (3.32), the incident mode power drops off exponentially along the perturbation region. This behavior, however, is not due to absorption but to reflection of power into the backward traveling mode A.

From (3.7) and (3.30) we find that the z dependent parts of the wave solutions in the periodic waveguide are exponentials with propagation constants

$$\beta' = \beta_0 \pm iS = \frac{l\pi}{\Lambda} \pm i\sqrt{\kappa^2 - [\beta(\omega) - \beta_0]^2} \tag{3.33}$$

where we used $\Delta\beta \equiv \beta - \beta_0, \beta_0 \equiv \pi l / \Lambda$.

A short section of a corrugated waveguide thus acts as a high reflectivity mirror for frequencies near the Bragg value, ω_0. The transmission

$$T_{eff} = \left|\frac{B(L)}{B(0)}\right|^2$$

and reflection

$$R_{eff} = \left| \frac{A(0)}{B(0)} \right|^2$$

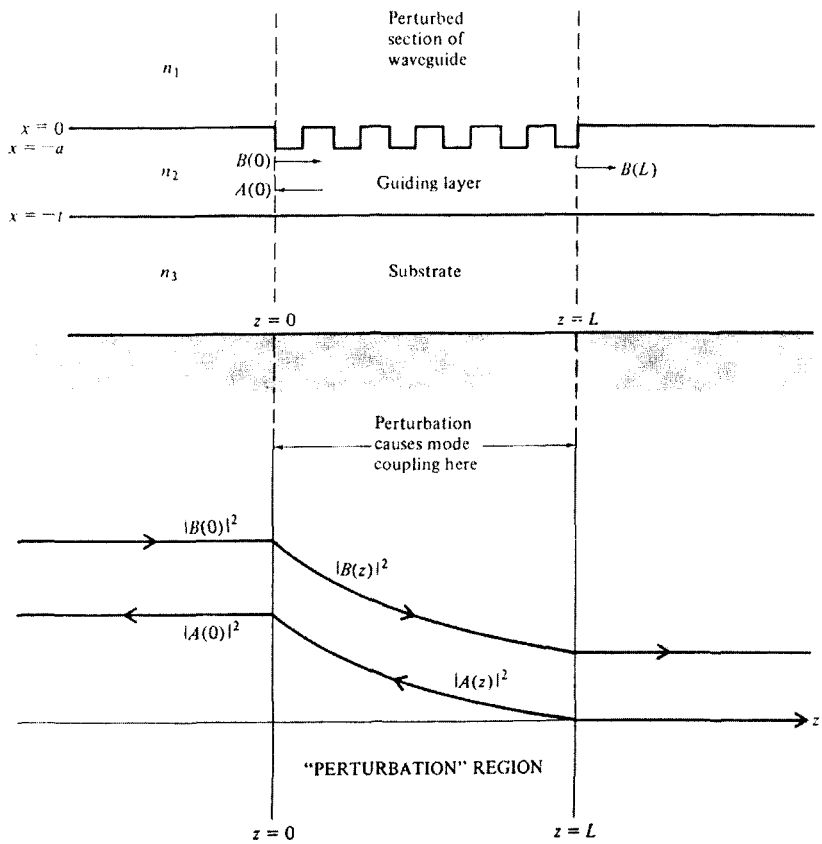

Figure 3-3 (upper) A Corrugated Section of a Dielectric Waveguide. The Incident and Reflected Intensities inside the Corrugated Section (lower)

CHAPTER 4 Grating Fabrication and Characterization

4.1 Grating Fabrication Techniques

All grating patterning performed in this thesis was done using a holographic system (i.e. by two beam interference). The steps required for grating patterning are illustrated in Figure 4-1 with further detail provided in Table 4-1. In brief, grating fabrication requires patterning, etching, cleaning.

The patterning for a grating is in many ways similar to patterning other structures. The main difference is the small scale of the grating features which introduce additional difficulties, especially in the determination of the quality of the patterning.

Before applying photoresist on the sample, precleaning is quite important for following processing procedure. The samples should be placed in UV ozone oven for 10 minutes to grow thin oxide films on silicon and then be put into buffered hydrofluoric acid for 30 seconds to get rid of the thin oxide films in order to remove organic contamination and modify surfaces for better adhesion. After precleaning procedure, photoresist is ready to spin on the samples. The photoresist (PR) used is Shipley 1808 which is a positive resist (i.e. exposed areas are removed during developing). Due to the small feature size, the PR is thinned in a ratio of 2:3 PR: thinner, and spun on at 5000rpm to ensure the formation of a thin layer of photoresist. After the photoresist is spun-on to the semiconductor surface, the sample undergoes a soft bake on a hot plate. (A soft bake is a low temperature bake required to partially cure the PR before the exposure is made.) Also, since the grating features are so small, the soft bake temperature is more critical. It is essential that the hot plate is allowed to stabilize at the correct temperature for at least 30 minutes.

If the hot plate is too cold, the PR won't set properly and too much of the PR will be removed during the development. Either way, the grating will be patchy. Even a 5 °C temperature variation is enough to noticeably affect the grating quality.

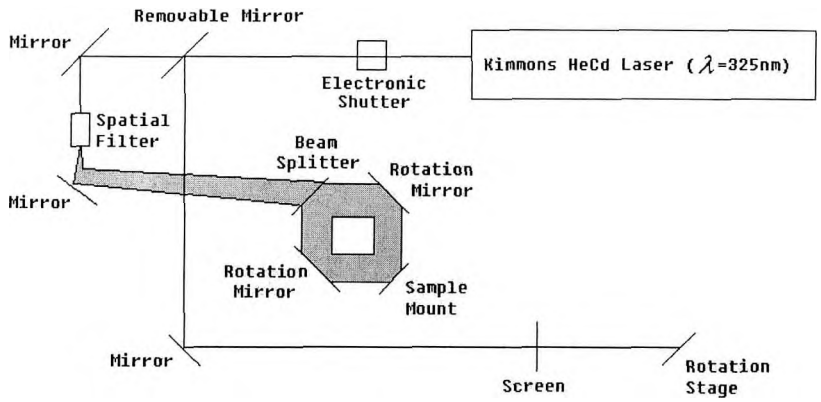

Figure 4-1 Illustration of Grating Fabrication System

With the soft bake completed, the PR is exposed in the UV holographic setup (Figure 4-1). The apparatus consists of a Kimmons HeCd laser which emits wavelength at 325nm, a spatial filter that ensures the beam uniformity and expands the beam, a beam splitter to form the two beams required for interference. Two rotating mirrors are used to redirect the beams onto the sample and to vary the grating period.

Normal exposure times are 60s for a 318uW/cm^2 arm power (i.e. the 1cm diameter detector measures 318uW in each arm). Ideally, both beams will have an identical power level to ensure that the nodes in the standing wave pattern formed from the interference have zero power and do not expose the photoresist. Both beams must be incident on the sample at the same angle from the normal otherwise the photoresist will develop with a non-uniform profile.

Step	Purpose/Comments
Allow HeCd Laser to warm up	
O_3 10 minutes	Cleaning sample step 1
BHF 30s	Cleaning sample step 2
Apply thinned PR	RP: Thinner 2:3
Spin PR at 5000rpm	PR thickness is approximate 80nm
Softbake 1 min at 80°C	Softbake temperature is critical
Expose in holographic system for 60s	Detector reading=318uW
Develop in Microposit CD30 developer for 80s	Slow agitation works best
Hardbake 2 minutes at 110°C	Prepare for etching grating
RIE etching 50s at 200W	CF_4: 30sccm O_2: 5sccm PR Etching rate: 80nm/min Si Etching rate: 30nm/min
Soak in Acetone for 5 mins	To remove PR
Rinse in DI	Cleaning sample

Table 4-1 Grating Fabrication Recipe

The grating period is varied by rotating the mirrors, and the beams are wide enough to provide adequate sample coverage for a quarter wafer. It is always preferable to move as few components as possible when system is properly aligned. The grating period is related to the diffracted angle by the equation

$$\Lambda = \frac{\lambda_{laser}}{2\sin\theta} \qquad (4.1)$$

where Λ is the grating period, λ_{laser} is the wavelength of the HeCd laser (which is 325nm), and θ is the measured diffracted angle. To change the reflection wavelength, one first calculates the required grating period (Λ) using the effective index of fundamental mode of SOI rib waveguide and the equation

$$\Lambda = \frac{\lambda_B}{2N} \qquad (4.2)$$

where λ_B is the Bragg wavelength, and N is the effective index of fundamental mode(N=3.48 for 4um ridge width SOI). The required angle of diffraction is then calculated from Eq.(4.1). The amount that each of the mirrors must be rotated is calculated by

$$\Delta\theta_{mirror} = \left| \frac{\theta_{current} - \theta_{target}}{2} \right| \qquad (4.3)$$

where $\theta_{current}$ is the current grating diffraction angle and θ_{target} is the target diffraction angle. To change the grating period, the mirrors are rotated in opposite directions: rotating the mirrors toward each other increases the grating period, rotating the mirrors away from each other decreases the grating period. The rotation of the mirrors must be controlled to a high degree of accuracy. For example, to change the reflection wavelength from 1550 to 1530nm, the grating period must be changed from 223 to 220nm (corresponding to diffraction angles of 46.7775° and 47.6154° respectively) which means that each of the mirrors must be rotated by only 0.4190°. Extremely tight control of the mirror angle is required for WDM applications where the reflection wavelength needs to be controlled to a fraction of a nanometer.

Development of the exposed photoresist is the next critical step after the exposure. The developer used is Shipley CD-30. The development procedure affects the amount of PR removed which will affect the grating pattern quality as illustrated in Figure 4-2. An underdeveloped pattern results in regions where not enough of the photoresist is removed, and an overdeveloped pattern results in areas where too much of the photoresist is removed. Hence, both an underdeveloped and an overdeveloped grating will result in regions where the grating is not etched properly into the semiconductor. Determination of the development time is relies on personal experience. We should observe the color change of the PR very carefully when the PR appears to be dark and then begin to be bright, we should stop the development process immediately and rinse the sample with distilled water. The amount and the uniformity of PR removed are affected by the amount of agitation of the sample during the development. A slow agitation appears to work best in my experience.

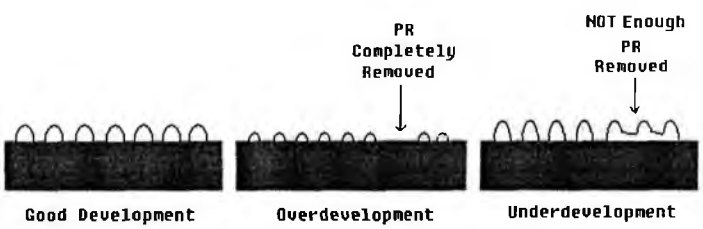

Figure 4-2 Schematic Diagram of Good Developed, Overdeveloped, and Underdeveloped Grating

After the development, the grating period is measured by using the rotation stage in Figure. 4-1 before etching. A HeCd laser wavelength sensitive paper screen with a hole in center is inserted in the optical path and a removable mirror is also inserted to direct the laser beam through the hole in the screen and onto the sample. With gratings on the sample, the sample will display a zeroth order diffraction pattern on the screen which is the principal maxima [18]. By noting the scale of the rotation stage, we will know the initial angle of principal maxima. Afterwards, we rotate the rotational stage clockwise and counter clockwise, and observe the $\pm$ 1 order diffraction pattern on the screen. By recording the scale of the rotation stage, the $\pm$ 1 order diffraction angle is obtained, respectively. Ideally, the $\pm$ 1 order diffraction angle should be identical, but in experiment, we add these two angles together and divided by 2 to achieve an average angle value, which is the θ value in Eq (4.1). Thus, by using Eq (4.1), we can determine if the grating period Λ is the desired value.

There are two methods for assessing the grating quality: atomic force images; diffraction from the grating using the light from a white light source, and from the HeCd laser.

4.2 Characterization Technique

4.2.1 Atomic Force Microscopy (AFM) Characterization

Since the AFM can resolve very tiny features as 5-10nm resolution, and show critical information about surface features with unprecedented clarity, the AFM is most accurate and advanced technology to characterize the quality of the gratings and determine the period and the depth of the gratings.

Like all other scanning probe microscopes, the AFM utilizes a sharp probe moving over the surface of a sample in a raster scan. In the case of the AFM, the

probe is a tip on the end of a cantilever which bends in response to the force between the tip and the sample. The first AFM used a scanning tunneling microscope at the end of the cantilever to detect the bending of the lever, but now most AFMs employ an optical lever technique. Figure 4-3 is schematic illustration about how a typical AFM works. As the cantilever flexes, the light from the laser is reflected onto the split photodiode. By measuring the difference signal (A-B), changes in the bending of the cantilever can be measured.

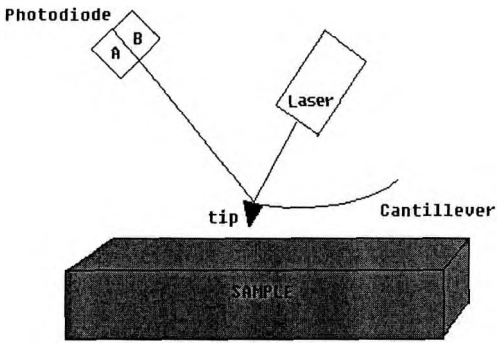

Figure 4-3 Schematic Illustration of AFM

There are three primary modes of AFM: Contact mode, non-contact mode and tapping mode. A tapping mode AFM was used in this work, which is the most common mode used in AFM. When operated in air or other gases, the cantilever is oscillated at its resonant frequency (often hundreds of kilohertz) and positioned above the surface so that it only taps the sample surface during scanning. This still involves a contact with the sample, but the very short time over which this contact means that lateral forces are dramatically reduced as the tip scans over the surface. When imaging poorly immobilized or soft samples, tapping mode may be a better choice than contact mode. Figure 4-5 and Figure 4-6 are the AFM images of gratings profile

and the SOI rib waveguide with gratings on its top. The grating pattern is first formed and then a rib waveguide is patterned by standard photolithology. This kind of process procedure is desirable, because conventional spin techniques lead to extremely uneven resist coverage as shown in Figure 4-4 if we fabricate rib first, which is problematic for grating patterning fine period structures.

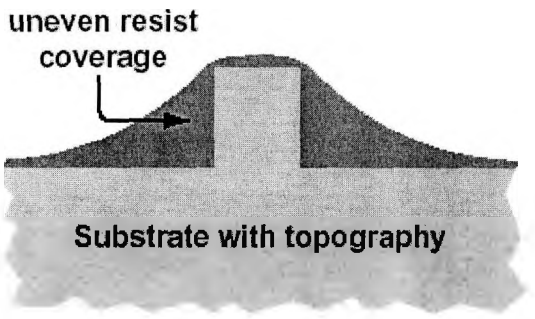

Figure 4-4 Schematic Diagram Illustrating the Problem with Performing Lithography over Topographic Features

4.2.2 Diffraction Pattern Characterization

The second method to check the quality of the grating is to use a white light source to inspect the diffraction pattern formed by grating. This kind of characterization technique can easily be used right after grating fabrication. The diffracted light should be a uniform blue color with the intensity of the diffracted light being proportional to the depth of the grating in the photoresist. Black regions signify areas of overdevelopment where the grating has been completely removed. However, if the grating appears too dazzling, the grating might be underdeveloped, not enough of the photoresist removed, which will result in a patchy grating after etching. Another test of quality of the grating pattern is the quality of the diffraction pattern obtained by using the beam from the HeCd laser. The diffracted spot should be uniform with very

few side fringes. If the diffraction pattern appears to have multiple side rings that means the sample is nonuniformly developed.

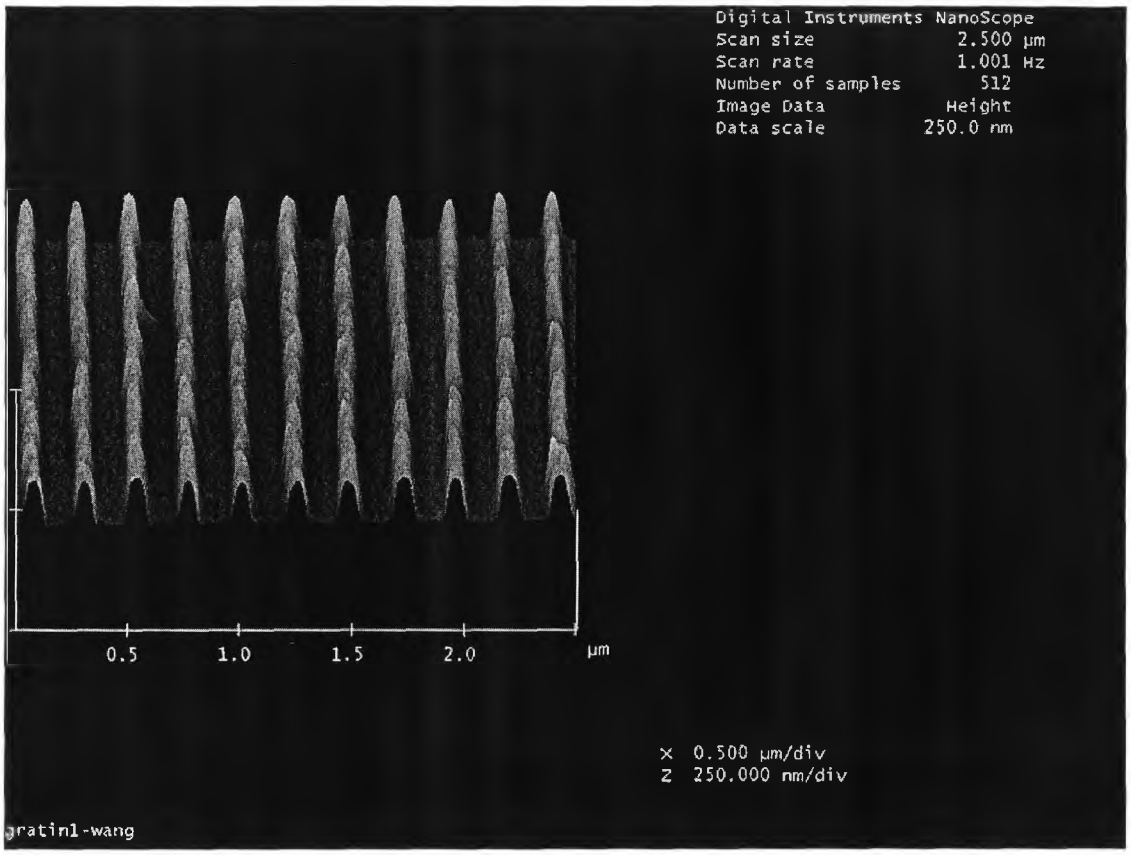

Figure 4-5 AFM Image of Grating Profile

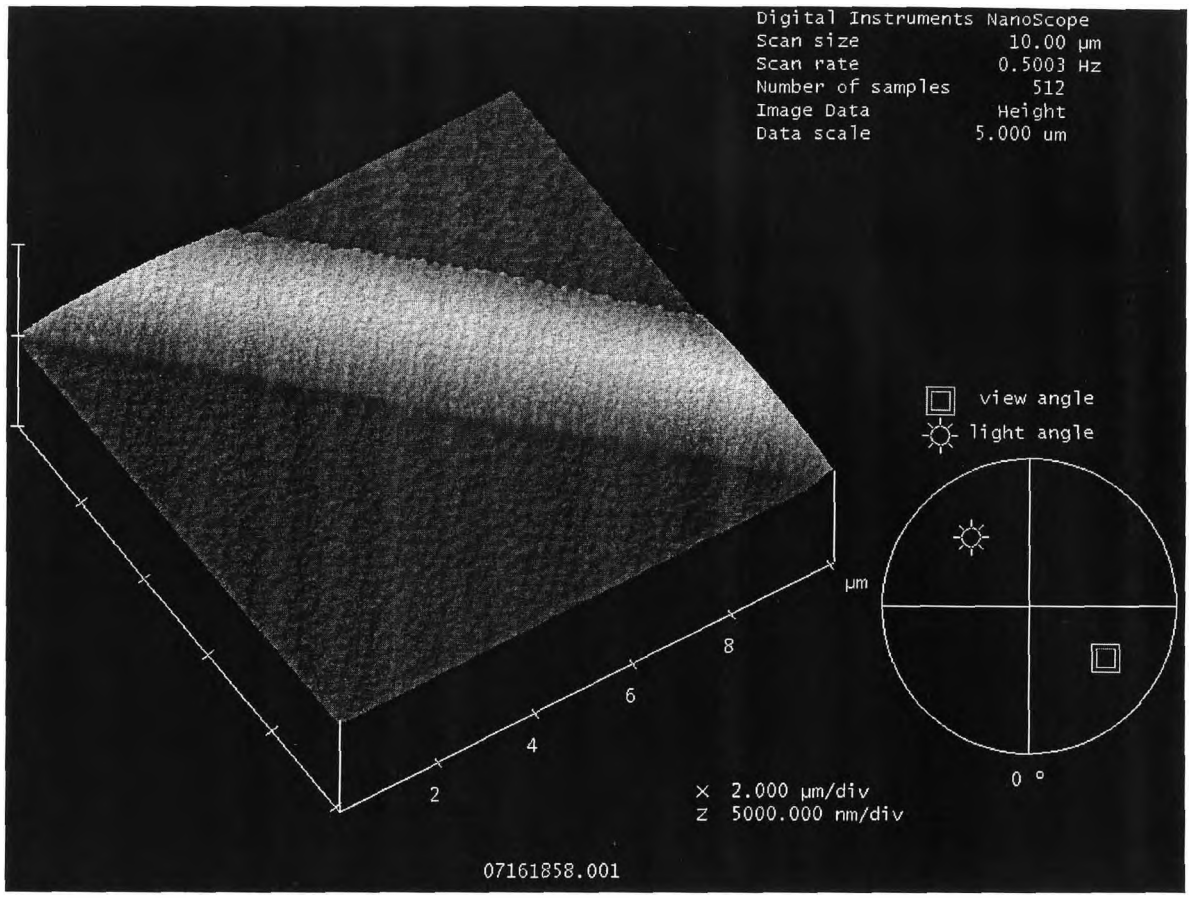

Figure 4-6 AFM Image of SOI Rib Waveguide with Grating Profile on its Top

CHAPTER 5 Experiment Results

The characteristics of the Bragg Grating on SOI Rib waveguide are discussed in this chapter.

5.1 Experimental Setup

An optical system, as shown in Figure 5-1, was set up on a floating optical bench to test the performance of the Bragg grating on a SOI wafer. A New Focus 6427 tunable laser was used as the wavelength tunable light source. The light was coupled into the chip by using a tapered fiber which was put through a polarization controller. The light emerging from the chip was collected with a 20× microscope objective lens and a linear polarizer was inserted to analyze the polarization of the light. CCD camera was used to ensure proper alignment and single mode operation.

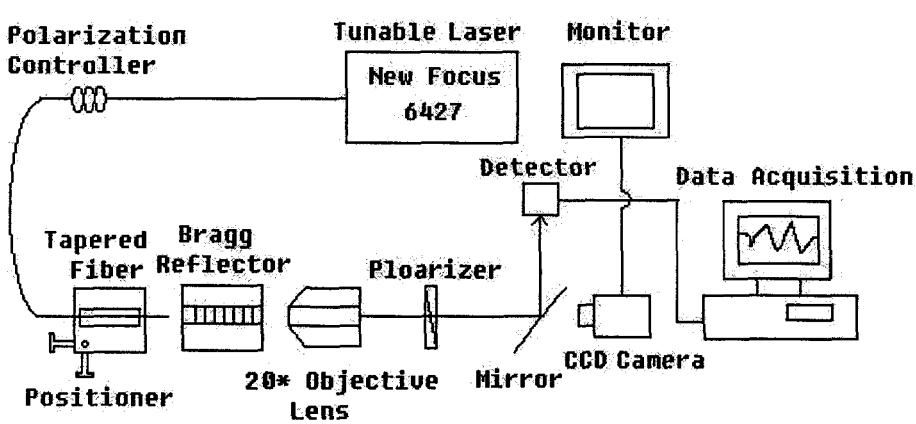

Figure 5-1 Experimental Setup Used to Test Bragg Grating Integrated on SOI Waveguides

5.2 Measurements

After the device was inserted and all the elements are aligned, the detected power decreased by approximately 16-20 dB. This insertion loss includes mode mismatch at the input facet, waveguide propagation loss, possible grating induced loss, Fresnel reflection at both facets. The theoretically calculated Fresnel reflection loss is around 6dB for both TE and TM mode. The 10 dB remaining loss is mainly believed as propagation loss. Although SOI has extremely low loss near λ=1.55um, the ridge waveguides have roughness and irregularities in the side walls which arise during lithographic and reactive ion etching processing. I anticipate that improvements to the fabrication sequence will lead to lower propagation loss.

Figure 5-2 depicts the measured transmission spectrum for a 1cm long Bragg grating. The transmission spectrum shows two distinct dips, and more might be present at shorter wavelengths that our laser could not reach. The first dip at 1518nm can be identified with grating assisted coupling between the forward traveling bounded fundamental mode and the backward traveling 1st higher order mode, whereas the final dip at 1532nm corresponds to the anticipated coupling from the forward to the backward guided fundamental mode. Since the designed grating pitch is 220nm, according to the Bragg condition as Eq. (5.1), with the fundamental mode index 3.48, we can calculate the reflection wavelength at 1531.2nm. Thus, the experimental result and the theory calculation are well agreed with each other.

$$2N\Lambda = \lambda \qquad (5.1)$$

where N is the effect index of fundamental mode, Λ is the grating pitch, and λ is designed reflection wavelength.

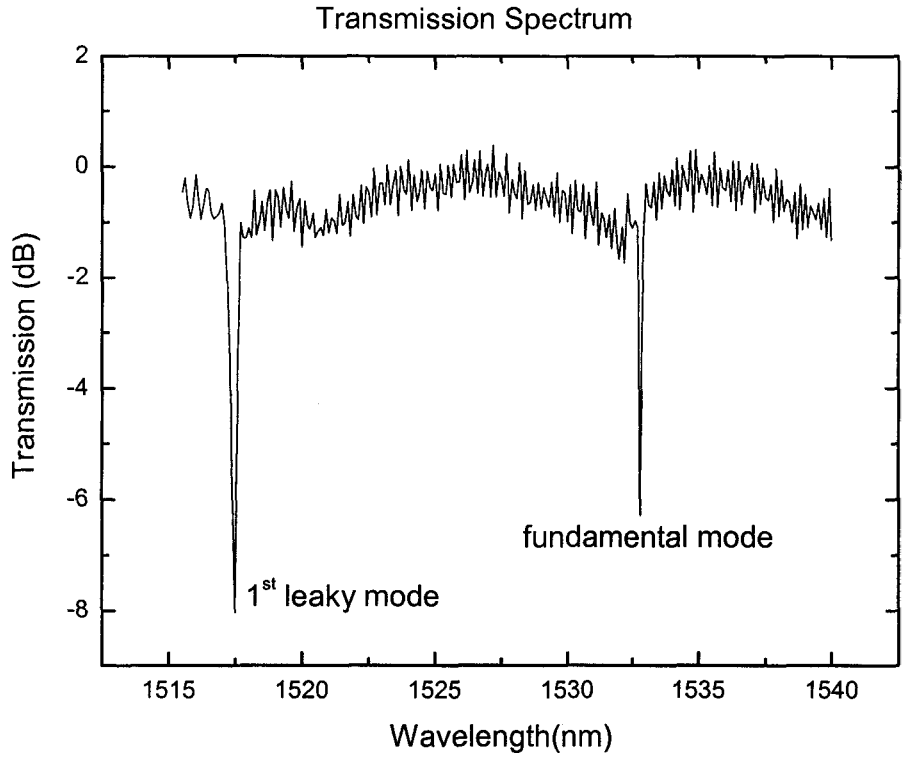

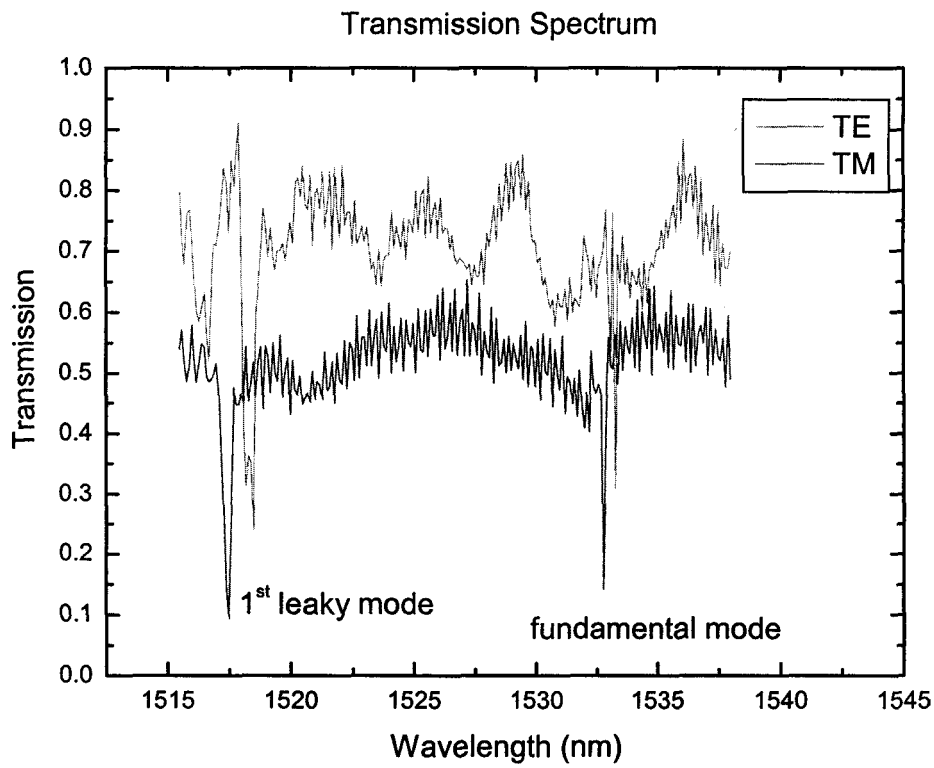

Figure 5-2 (a) Measured TM Transmission Spectrum for Bragg Gratings

(b) Measured TE & TM Transmission Spectrum for Bragg Gratings

5.3 Explanation of Higher Order Dips [19]

With the grating on top of the ridge waveguide, the Bragg grating creates a coupling between the modes wherever the difference between their propagation constants is equal to the vector of the grating as follows, which is called phase matching condition:

$$\beta_n(\lambda) - \beta_m(\lambda) = \frac{2\pi}{\Lambda} \qquad (5.2)$$

where the Λ is the period of the Bragg grating, n and m are corresponding to the order of modes. Conventionally, positive values of β correspond to forward traveling modes, while negative values correspond to backward traveling modes.

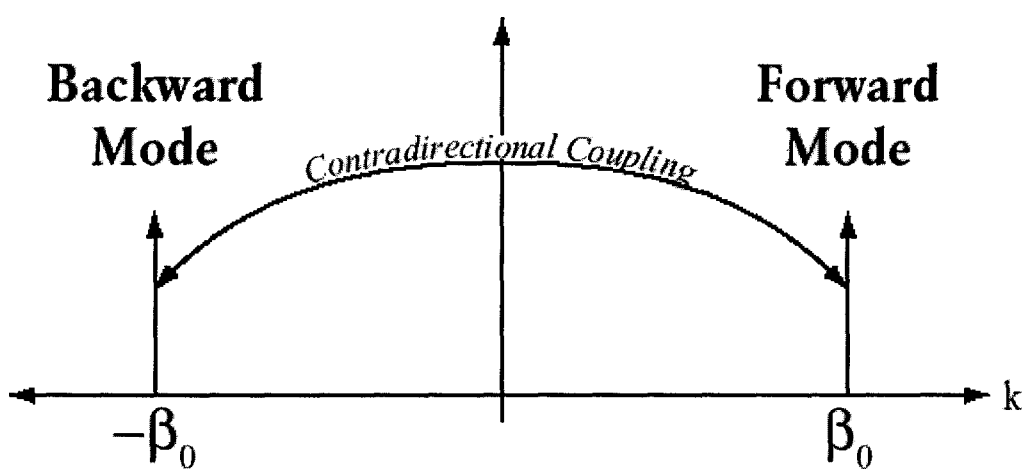

Figure 5-3 Coupling Energy between the Forward and Backward Traveling Modes

If a grating with wave vector $2\beta_0$ is added to the waveguide, it can couple the forward and backward traveling waves because the difference in propagation constant between the forward and backward traveling fundamental modes is precisely $2\beta_0$.

Figure 5-4 depicts the calculated dispersion relation (β vs λ) for the first four TE modes of slab SOI structure. The negative propagation constants correspond to the lowest four backward traveling modes. The Bragg grating creates a coupling between

the modes wherever the difference in propagation constants satisfy Eq. (5.2). The two arrows drawn in Figure 5-4 illustrate the two wavelengths at which light from the forward traveling fundamental mode can be coupled to a backward traveling mode.

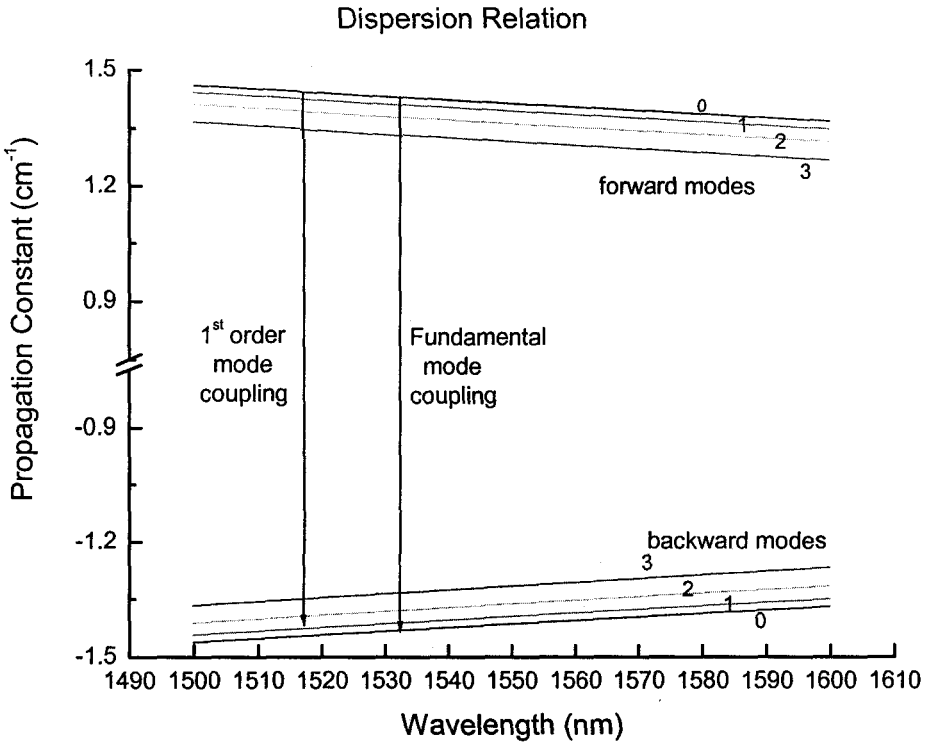

Figure 5-4 Dispersion Diagram of SOI Waveguides

At wavelength 1518nm, the forward traveling fundamental mode has been coupled to the first higher order mode which will propagate backward bound. Since our rib SOI waveguide only supports fundamental mode propagation, this higher order mode can not be supported by the rib SOI waveguide, and it will quickly radiate into side region as propagating backward. Thus, at wavelength 1518nm, there is a dip corresponding to the 1st order leaky mode. Since all the higher modes are leaky, we can associate the higher order modes with leaky modes. At lower wavelength, there should be more

dips corresponding to the 2nd, 3rd order leaky modes, where our laser wavelength can not reach. But in the next chapter, with the computer simulation, we can precisely identify the wavelength at which the dips will occur.

Observed from the transmission spectrum, the 1st leaky mode linewidth is wider than the fundamental mode. This is an interesting phenomenon. For the fundamental mode, all scattered components will add constructively, and the linewidth will be narrowest. For higher order modes, although they are phase matched with fundamental mode, and there will still be scattered components, these scattered components will sum with slight different phases. The higher the order mode, the greater the difference involved, and there will be wider linewidth.

The reflection strength of different modes is also varying. This is due to variations in the overlap integral of the higher modes with the fundamental mode over the grating region. Initially, all the modes are orthogonal. This means that an integral over the whole guide cross section, of a product of the transverse field of two modes, is zero. And any two modes will not have energy exchange. But with the grating existing, the boundary condition has been changed, and grating will introduce net overlap integral sections between two modes. Therefore, energy can be transferred from one mode to another, and if the overlap integral section is larger, the reflection strength will be stronger.

5.4 Polarization Dependence of SOI Rib waveguides [20]

As depicted in Figure 5-2 (b), TE and TM peaks are separated by 1nm, which shows the birefringence effect. Silicon is not an intrinsically birefringent material. The main source of birefringence is from the rib waveguide structure. Rib waveguides, unlike circular waveguides or square waveguides, do not have a symmetrical

geometry. This will result in different confinement of two perpendicular polarization, TE and TM modes. This birefringence problem is an intrinsic drawback associated with rib SOI waveguides. We can minimize this effect by using a deep etch in the rib waveguide, but if we etch the rib too deep, the higher order modes will also be confined. It will contaminate the transmission spectrum. Moreover, if we etch the rib too deep, the grating perturbation on top of the rib will be weak and this will result in shallow dips. In the next chapter, I will discuss the optimization of Bragg gratings integrated on SOI rib waveguides.

5.5 Fiber PIC coupling [3]

Silicon on Insulator (SOI) materials are high index contrast (HIC) waveguiding materials that enable the dense integration of many devices on single photonic integrated circuit (PIC). A major disadvantage of this approach is the difficulty of coupling light into and out of an optical fiber. Approximating the fiber mode by a Gaussian distribution, the mode field diameter (MFD) of a fiber is defined as the $1/e^2$ diameter of the Gaussian power distribution and is approximately 15% larger than the core diameter. The typical MFD of a single mode fiber is 8-10 um and the mode cross section is ideally circular. A tapered fiber has a typical output beam diameter ~50% of the typical MFD and ~20 um focal length. A HIC waveguide has a mode profile in the micron range and the mode cross section is highly elliptical. The large mode mismatch leads to very inefficient fiber-waveguide coupling with most of the power lost to radiation. The coupling loss between fibers and waveguides, assuming that they are perfectly aligned [21], is:

$$\text{Loss (dB)} = -10\log\left\{\frac{4}{\left(\frac{MFD_1}{MFD_2}+\frac{MFD_2}{MFD_1}\right)^2}\right\} \qquad (5.3)$$

If we ignore the ellipticity of a waveguide mode and apply (5.3) to get an estimate for the coupling between a tapered fiber and a waveguide with 5:2 MFD ratio, we can find 3.2 dB loss.

Other loss mechanism can be attributed to the Fresnel reflection. At each facet between silicon and air, there will be reflection loss. Assuming fiber and PIC are properly aligned, and at normal incidence, for both TE and TM modes will have reflection loss according to (5.4)

$$R = \left(\frac{1-n}{1+n}\right)^2 \qquad (5.4)$$

With the refractive index n=3.5 of silicon, and air index 1, we can calculate the Fresnel reflection R=0.30864. This value of R corresponds to a reflection of 30.864 percent of the emitted optical power back into to air. Given that

$$P_{coupled} = (1\text{-}R)\, P_{source} \qquad (5.5)$$

The power loss L in decibels is found from following formula:

$$L = -10\log\left(\frac{P_{coupled}}{P_{source}}\right) = -10\log(1-R) = -10\log(0.691358) = 1.6\text{dB}$$

At both facets, the loss will be doubled as 3.2 dB. In summary, 6.4 dB loss is expected for 2.2um SOI rib waveguide resulting from mode mismatch loss and reflection loss. Other loss mechanism can be mainly attributed to rib waveguide surface roughness, I expect to use ECR-RIE, and Cl_2 to etch the rib waveguide in the future, which will greatly improve the surface smoothness.

CHAPTER 6 Computer Simulations and Optimization

6.1 Introduction

In this chapter, we will discuss the various parameters which will influence the performance of the Bragg Grating Reflector by using MATLAB software package. Furthermore, we can use the computer simulation to come up with better proposals to design optimized devices. The fundamental scheme of computer simulation is presented as Figure 6-2 and source MATLAB codes are listed in appendix A. The main computer simulation scheme is based on coupled mode theory (CMT). [23] [24] [25]

6.2 Variation of Grating Period

Since we use the holographic system to fabricate the grating on top of the SOI waveguides, not like e-beam lithography, it is difficult to change the grating period by 1 nm per step. But using computer simulation, we can investigate the effects of varying of grating period. The following waveguide parameters are used: n_c=1(air), n_f=3.5(silicon), n_s=1.5(SiO_2), grating depth=80nm, grating length L=1 cm, top silicon thickness=2.2um.

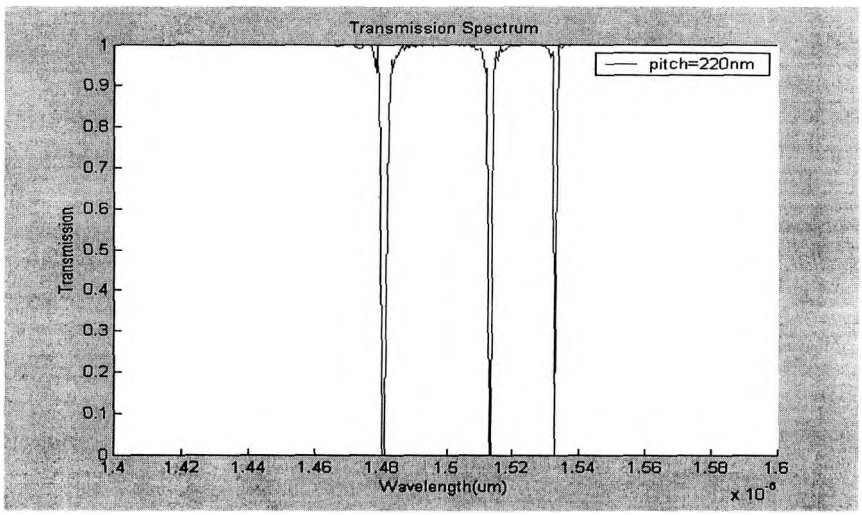

Figure 6-1 Simulation of Transmission Spectrum of 2.2 um SOI
(a) Grating Pitch=220nm

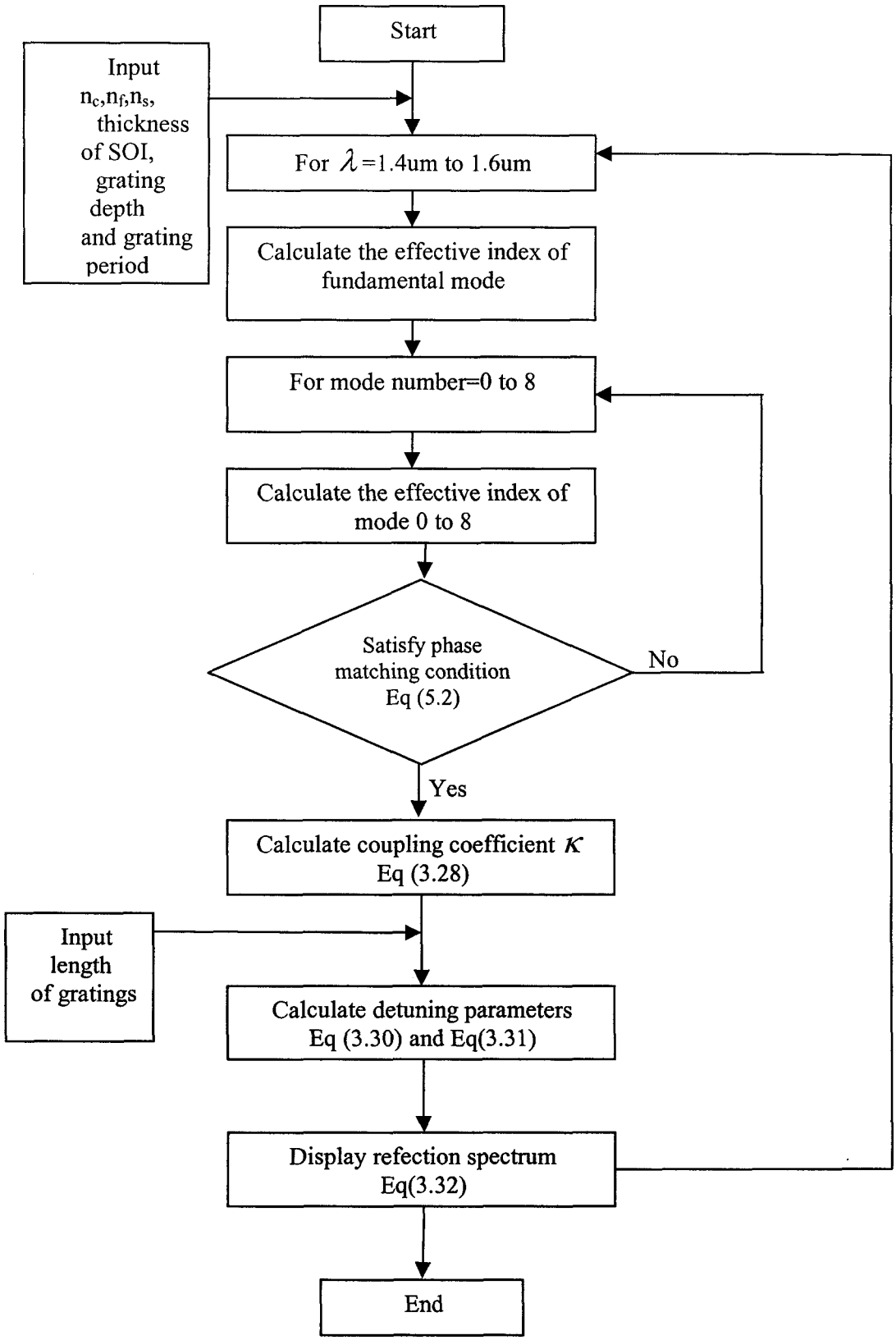

Figure 6-2 Computation Diagram of Simulation

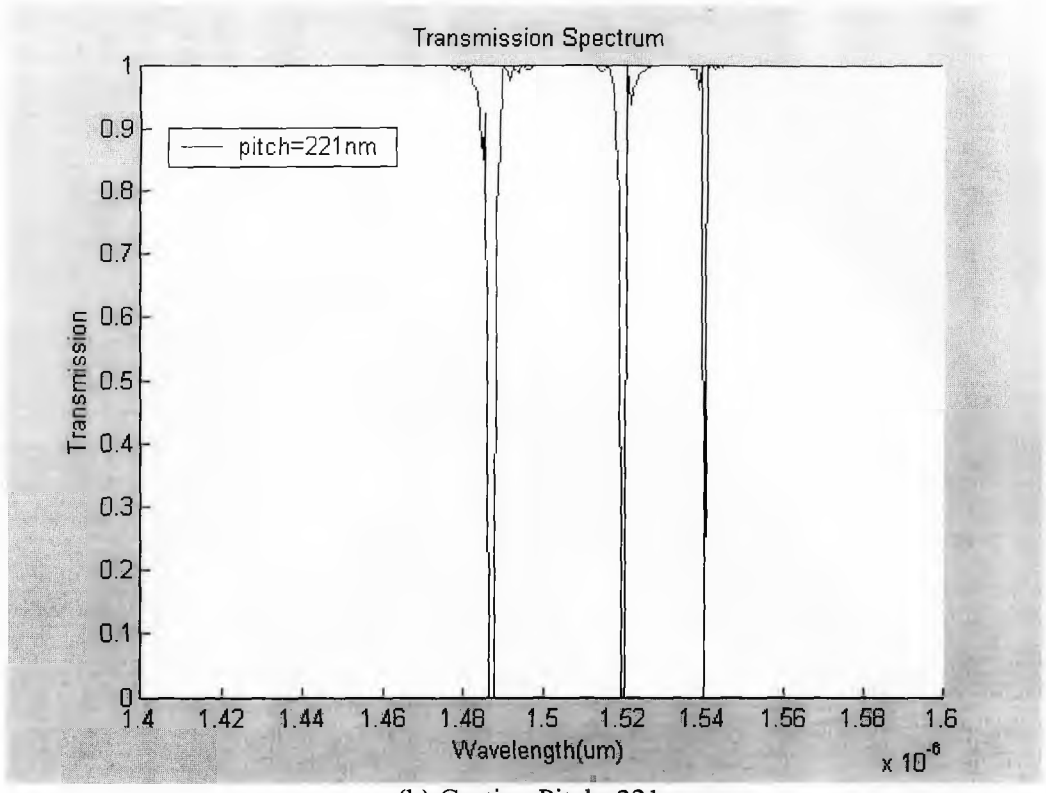

(b) Grating Pitch=221nm

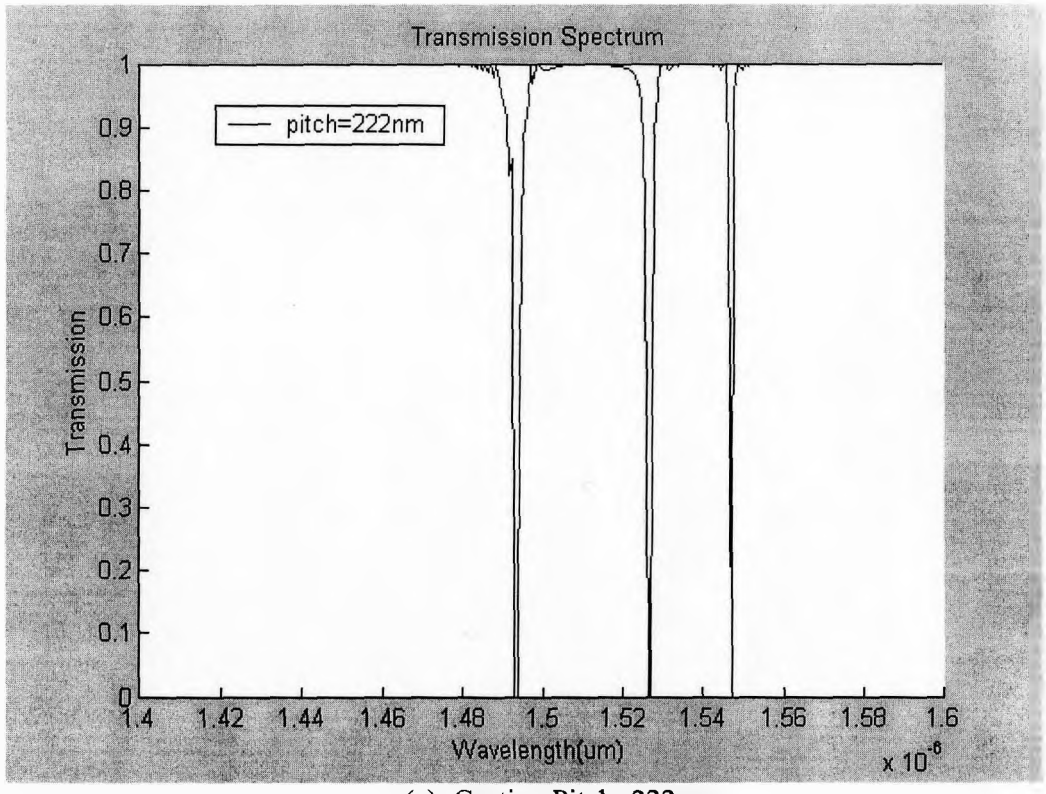

(c) Grating Pitch=222nm

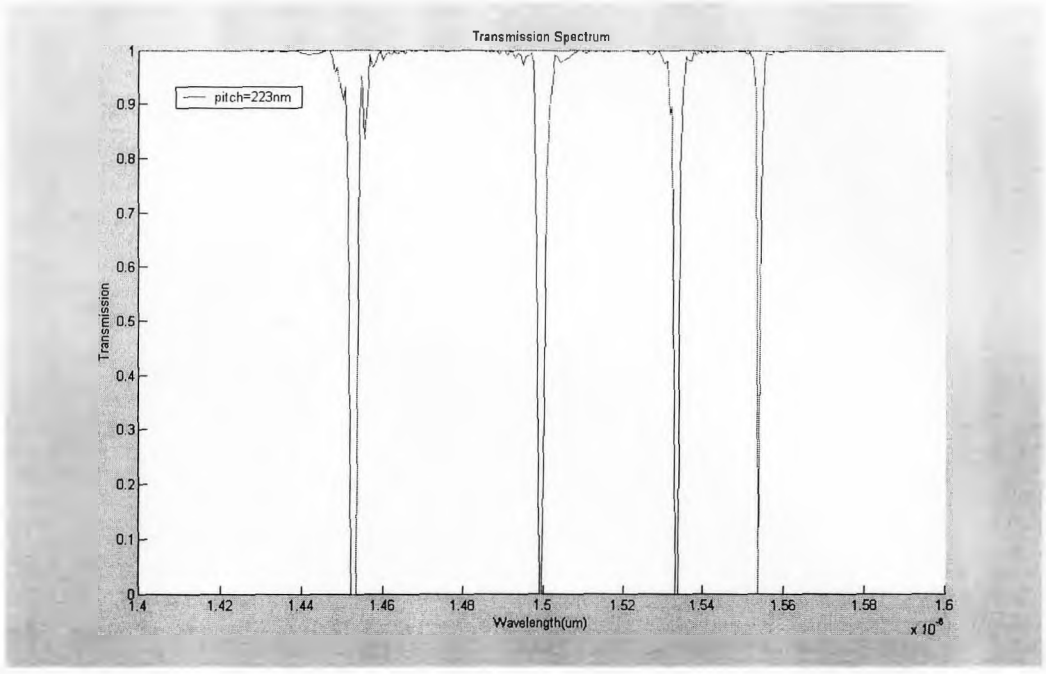

(d) Grating Pitch=223nm

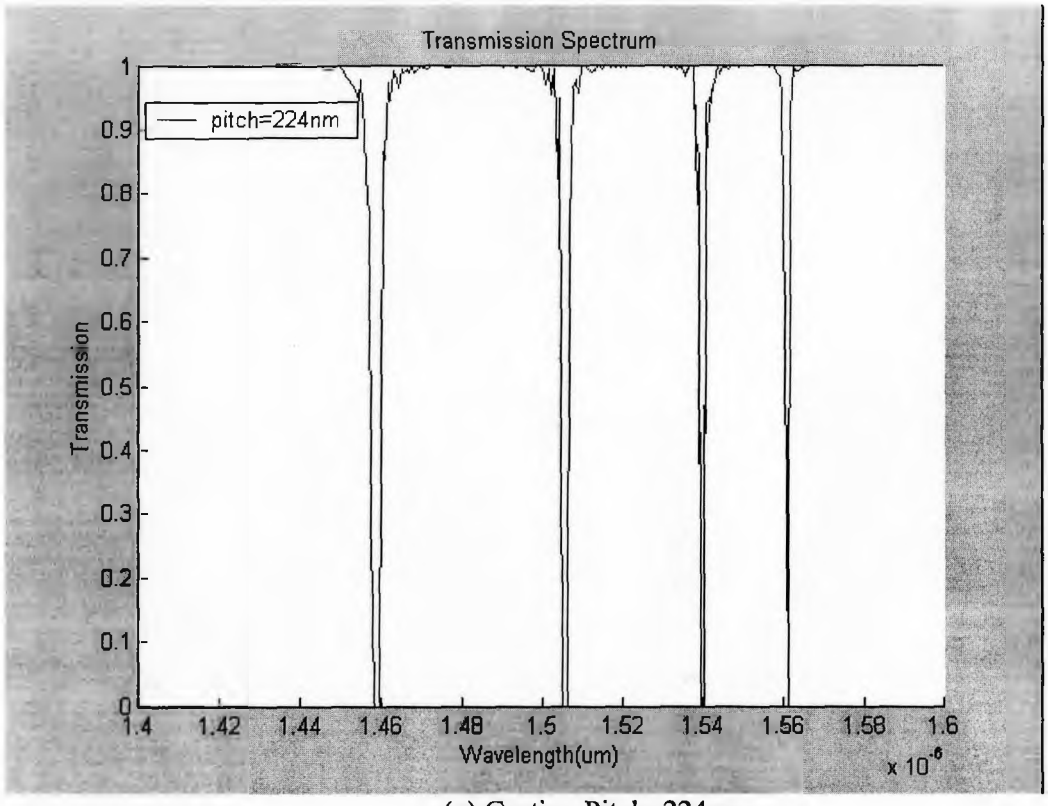

(e) Grating Pitch=224nm

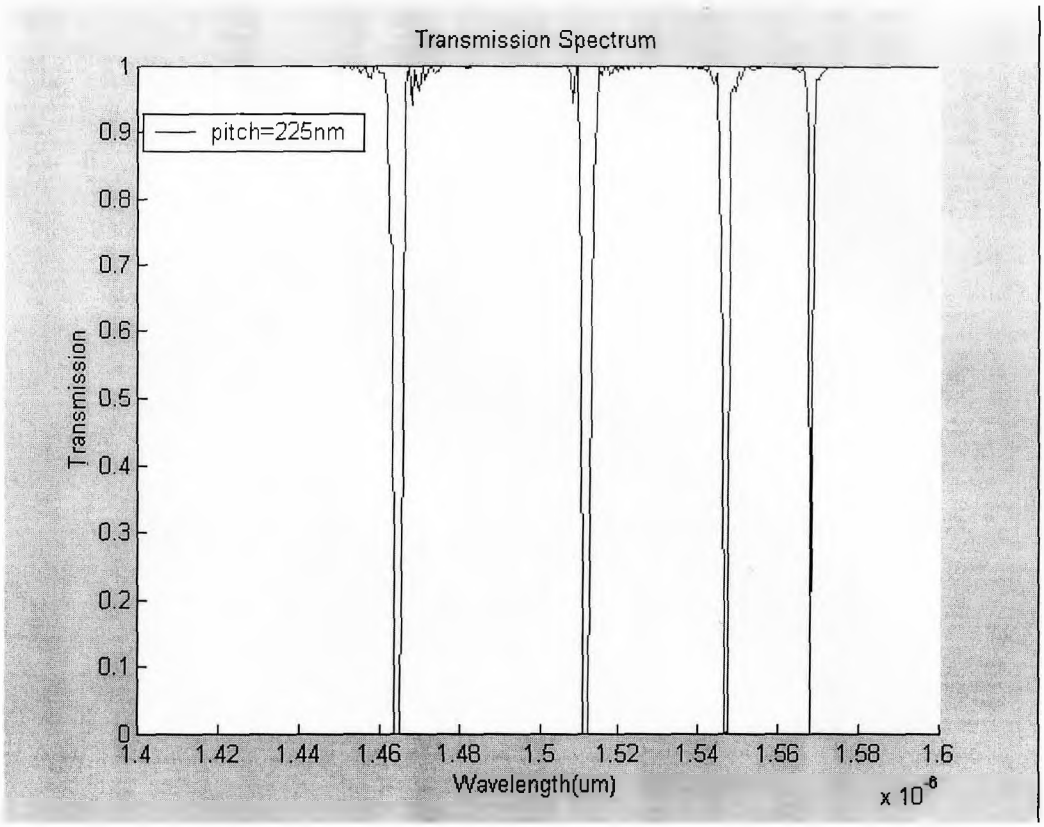

(f) Grating Pitch=225nm

Figure 6-1 Simulation of Transmission Spectrum of 2.2 um SOI

It can be seen in Figure 6-1, when we consider the effective index of fundamental mode is 3.48 and the grating period is varying from 220nm to 225nm, the Bragg Reflection wavelength shifted from 1531nm to 1566nm. Figure 6-1 (a) is of particular interest, because the computer simulation result agrees qualitatively with the measured data presented in Figure 5-2, in spite of the simplifying approximations made (i.e., replacing the ridge with a slab). The fundamental mode reflection appears at 1531nm, the 1st higher order mode reflection appears at 1518nm. Since our tunable laser can not reach wavelength below 1500nm, there are only two dips presented on the transmission spectrum. With Figure 6-1 (a), we can predict there should be the third dip at wavelength around 1480nm, which is corresponding to the fundamental mode coupled to the second higher order mode. Since using holographic lithography

to fabricate Bragg grating, precise control of the grating period is quite difficult. The wavelength range of the tunable laser that we use to test chips is 75nm, from 1500nm to 1575nm. This requires the grating period between 215nm to 226nm, only an 11nm range; otherwise, we can not observe dips on the transmission spectrum. Using the computer simulation, we can easily determine which grating period is appropriate for device application.

With the Grating period increased, another effect that we observe is that at lower wavelength there are more dips due to the fact that more higher order modes will satisfy the phase matching condition, and the coupling between fundamental mode to higher order modes will happen. The strength of reflection is mainly dependent on the overlap integral between the fundamental mode and the higher order mode over the grating region.

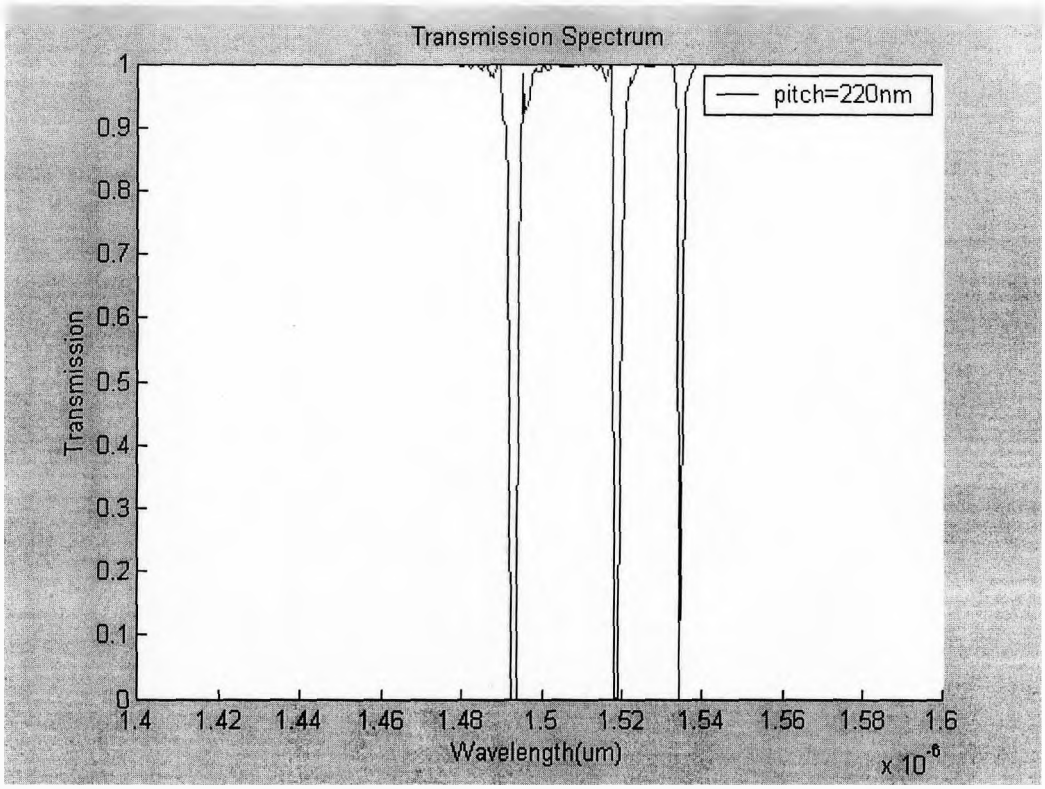

Figure 6-3 Simulation of Transmission Spectrum of 2.5 um SOI
(a) Grating Pitch= 220nm

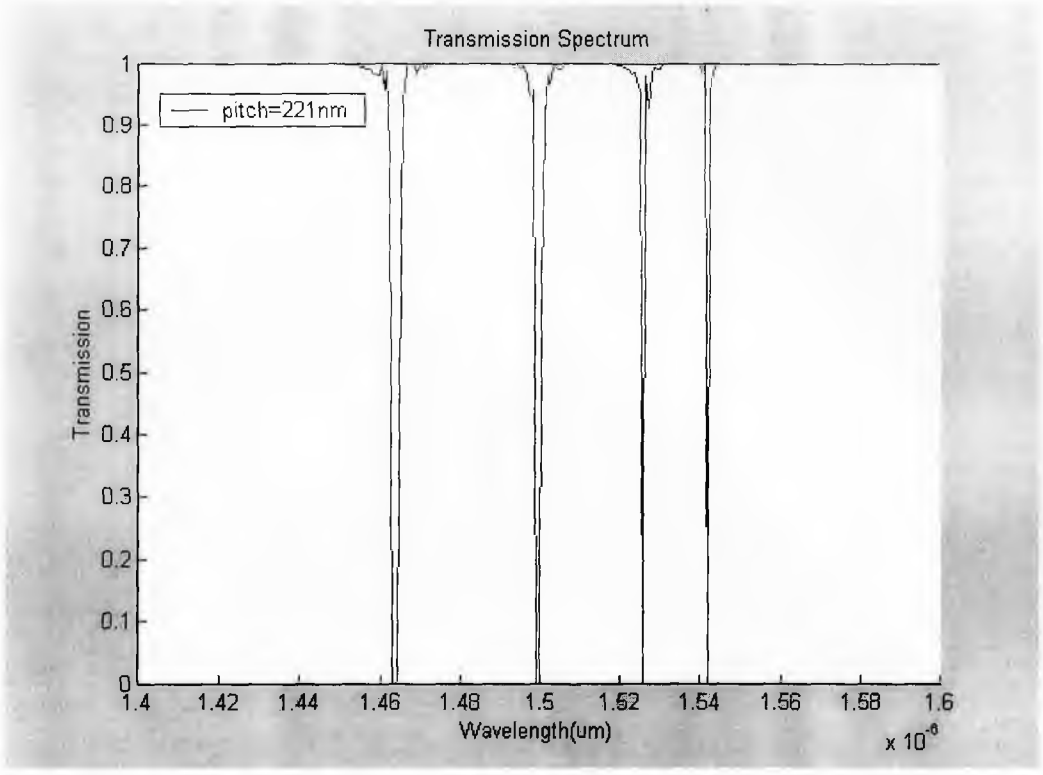

(b) Grating Pitch= 221nm

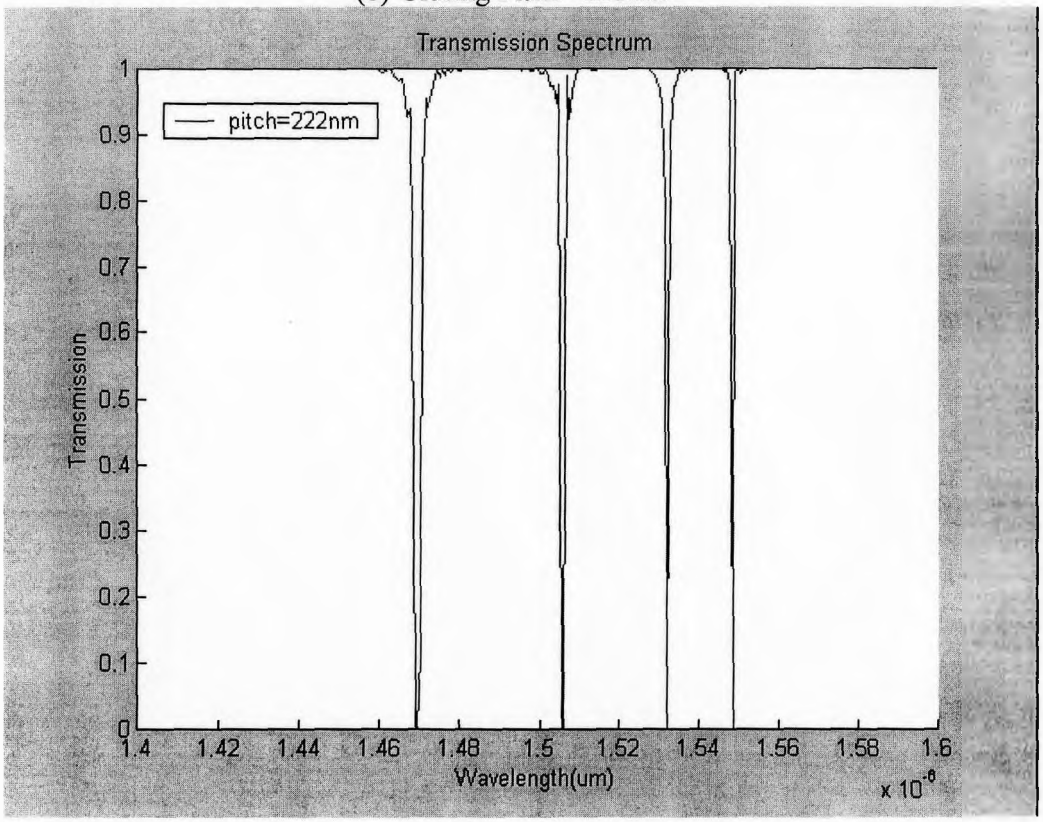

(c) Grating Pitch= 222nm

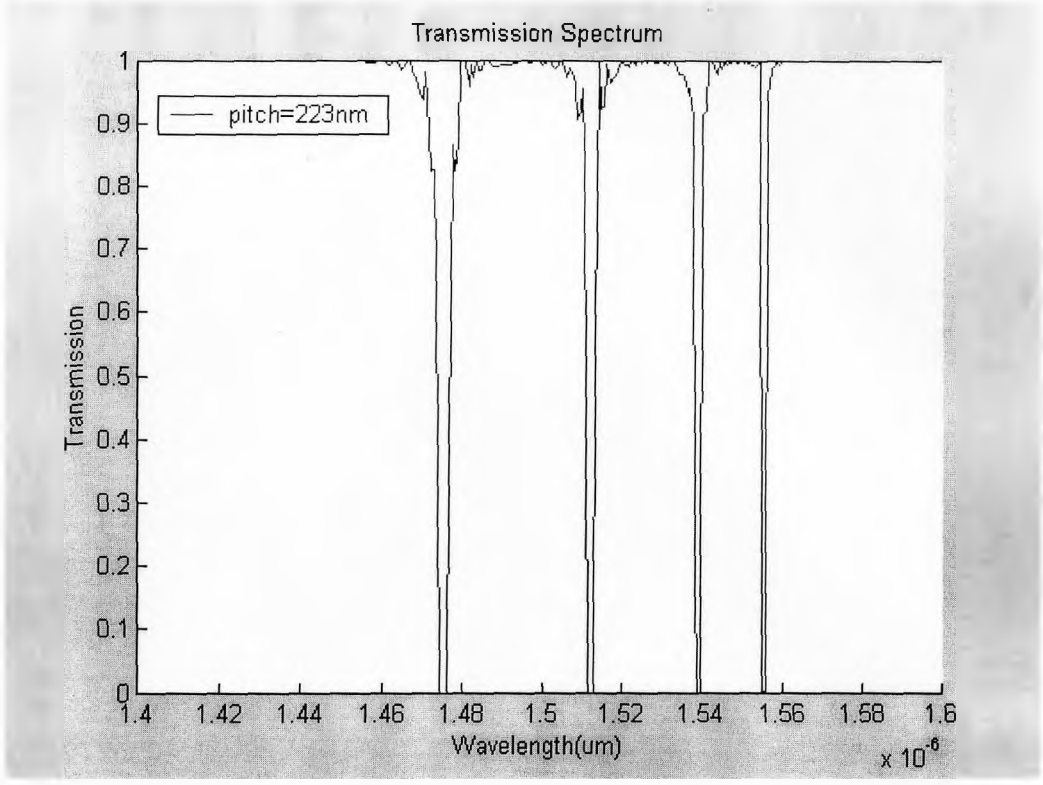

(d) Grating Pitch= 223nm

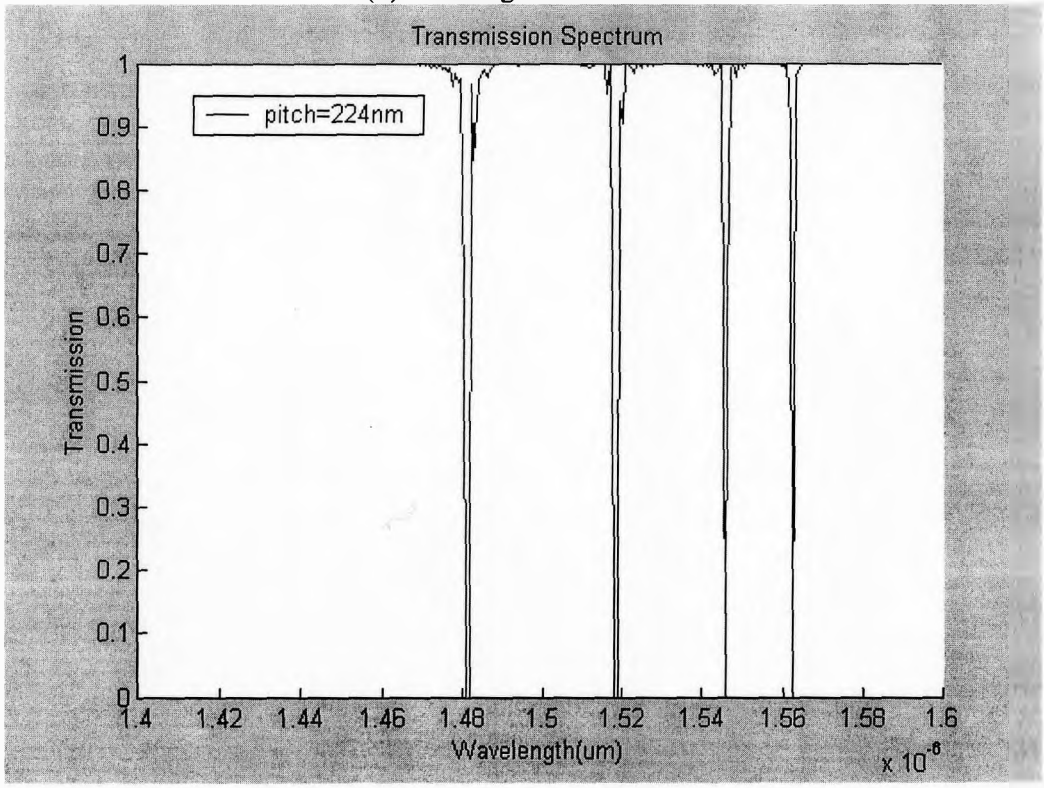

(e) Grating Pitch= 224nm

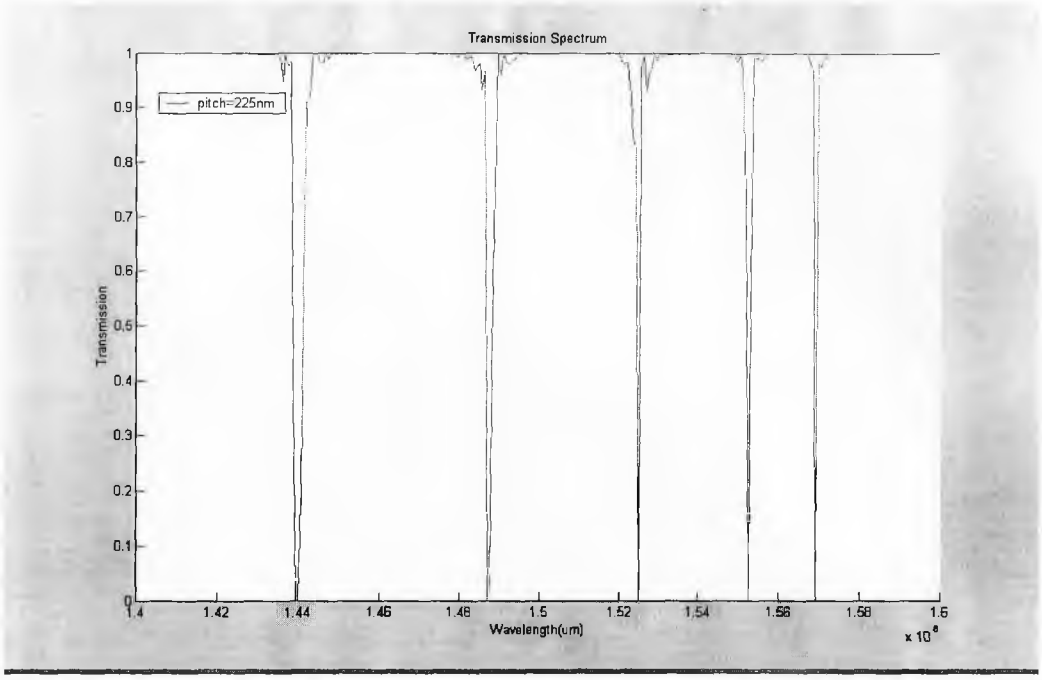

(f) Grating Pitch= 225nm

Figure 6-3 Simulation of Transmission Spectrum of 2.5 um SOI

Compared with a 2.2um thick SOI waveguide, a 2.5um thick SOI waveguide has 4 distinct dips with the grating pitch 221nm. This result illustrate that with thicker guiding layer, more mode numbers can be supported, and grating will readily assist coupling from fundamental mode to higher order modes.

6.3 Variation of Grating Depth

The effect of grating depth on SOI waveguide has also been investigated. The top silicon thickness is 2.2 um with the grating length of 1cm.And the transmission spectrum of grating depth of 60nm, 70nm, and 80nm are shown in Figure 6-4.

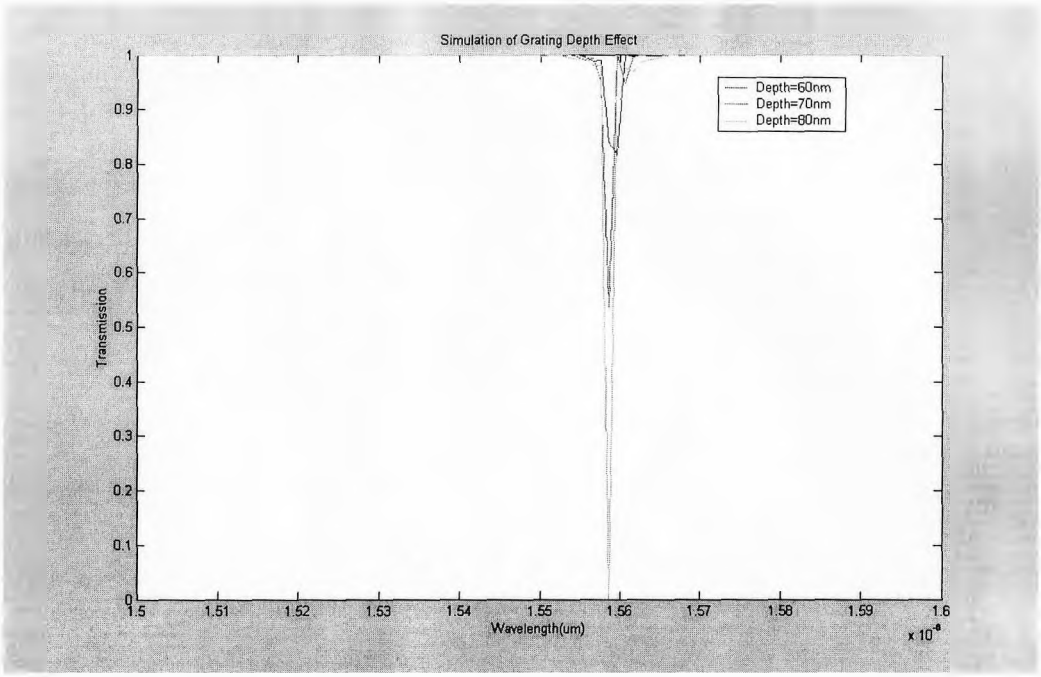

Figure 6-4 Variation of Grating Depth on 2.2 um SOI Waveguide

As presented from Figure 6-4, 60nm deep grating will reflect 25% of the optical power, 70nm deep grating will reflect 50% of the optical power, and 80nm deep grating will reflect 100% optical power. The grating depth effect is dramatic in determining reflection strength, deeper etching of the grating will increase the coupling coefficient κ (2.5424e3, 3.2807e3, 4.1293e3 for the three etch depths presented in Figure 6-4) and results in strong reflection. Another useful aspect of Figure 6-4 is we can determine the saturation reflection strength of grating depth. As we etch grating deeper and deeper, there should be a maximum of reflection. From simulation, we can see with 80nm grating depth, the reflection will approach 100%.

This computer simulation is based on a slab waveguide, in a real device we have ridge waveguide and the electrical field of mode will penetrate into the rib region. And gratings on top of the rib waveguide will create a stronger perturbation than slab waveguide. Thus, with even shallow grating depth perturbation will achieve the maximum reflection.

6.4 Variation of Grating Length

Grating length is also an important parameter that we should consider in research work. Three cases with 0.5cm, 1cm and 1.5cm long and 60nm deep gratings are studied as follows:

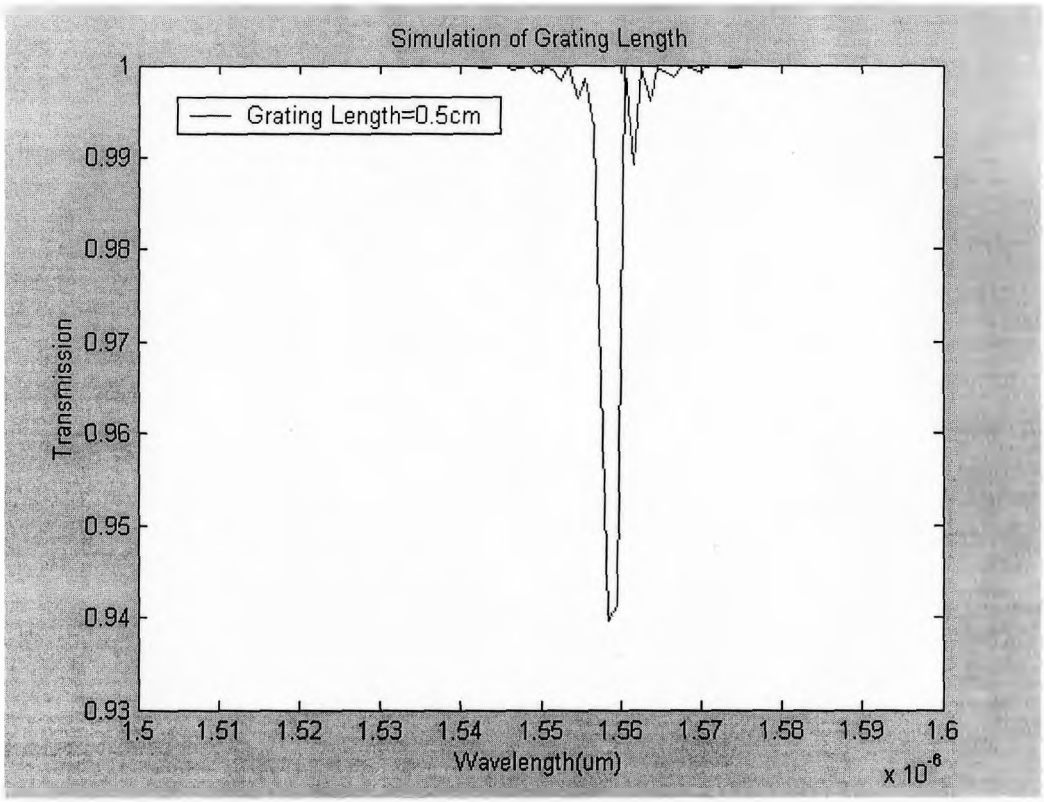

Figure 6-5 Variation of Grating Length on 2.2 um SOI Waveguide
(a) Grating Length=0.5cm

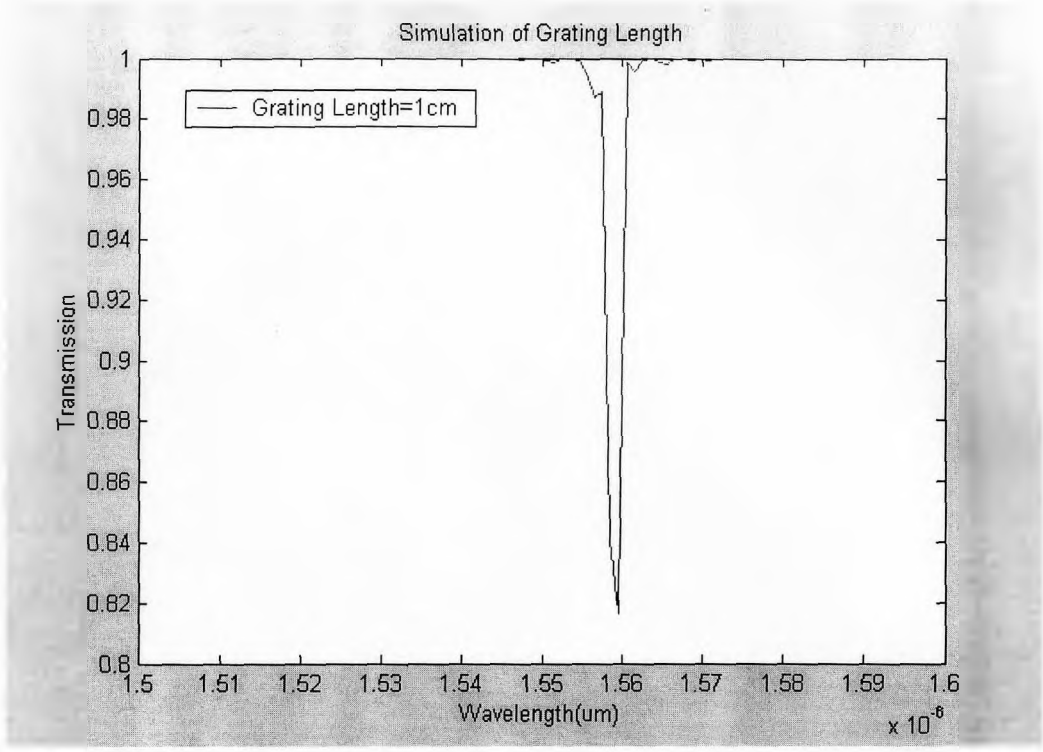

(b) Grating Length=1cm

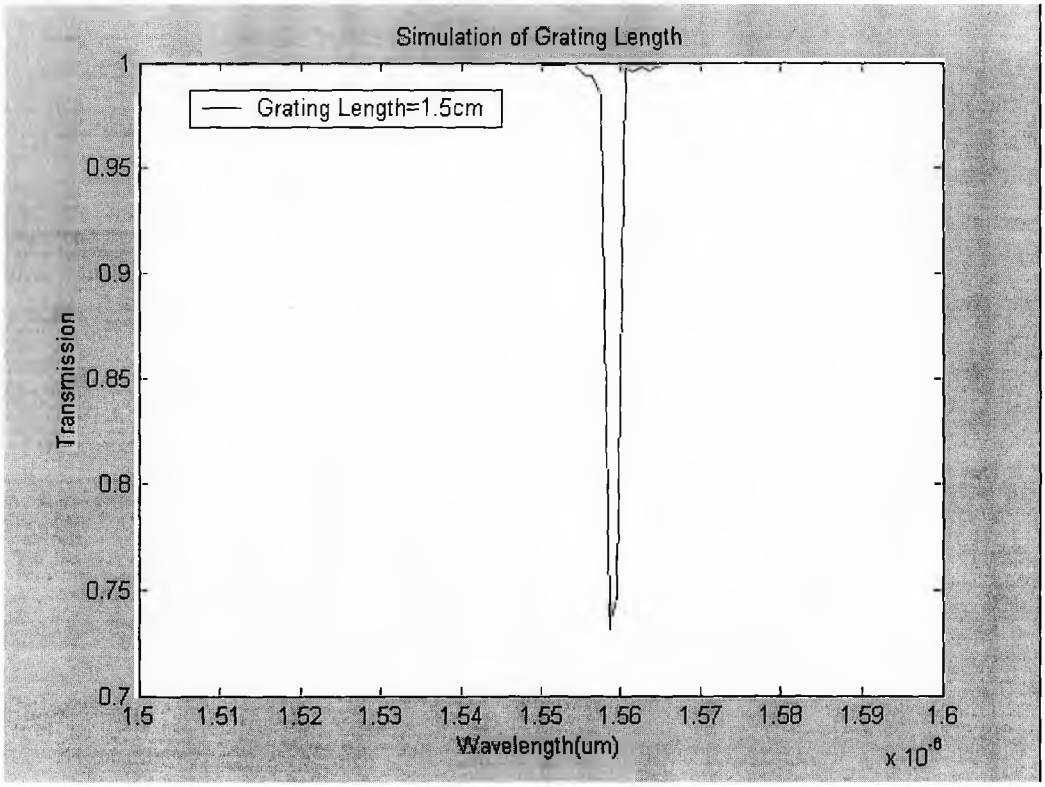

(c) Grating Length=1.5cm

By increasing the length of Bragg grating, the reflection strength will increase and the linewidth of the reflection will be narrower, which demonstrate the good wavelength selectivity. But increase grating length will increase the device size and device will experience more propagation loss due to the roughness of the sidewall. Furthermore, compared to the grating depth effect, increase grating length is not a salient method to enhance reflection. In a general sense, most of the energy is concentrated in the center of the rib waveguide, so make deeper gratings will effect more energy portion, and cause powerful perturbation. Therefore, if other parameters are limited due to fabrication restricts, we can increase grating length to achieve strong reflection, but it is a better way to increase grating depth to obtain strong reflection.

6.5 Device Optimization

In summary, all the grating parameters have been explored to observe the influence on reflection by computer simulation. Utilizing these results, we can conclude that the best grating structure on 2.2 um SOI should have 222nm grating pitch, 80um depth, and rib waveguide width could be 4 um and rib depth could be 0.26um.

CHAPTER 7 Conclusions

This thesis describes the design, fabrication, measurement and modeling of an integrated optical Bragg grating filter, based on a silicon on insulator (SOI) ridge waveguide, which demonstrates the potential application for DWDM communication system.

Narrow band optical wavelength filters are building blocks for the DWDM system. A periodic grating in an optical waveguide is often used to provide an efficient mode coupling mechanism in narrow band filter design. [26] Furthermore, with the emergence of the SOI material system, we want to explore the possibilities of combining Bragg grating on SOI material which is fully compatible with silicon processing technology. [27]

Our observations show that a nominally single mode ridge waveguide can have higher order leaky modes with the existence of a grating, which lead to a loss mechanism on the short wavelength of the transmission spectrum. Although radiation loss is an undesirable effect for add/drop filters, it might be possible to exploit this effect for other applications such as gain equalization. With computer simulation that we designed based on coupled mode theory (CMT), we can quantify the transmission spectrum and predict the leaky mode wavelength. This can lead us to optimize the device structure and achieve the desirable wavelength for system design. Furthermore, all the grating parameters are investigated by computer simulation, which will give us a clear knowledge of what is the most salient influence upon coupling coefficient and reflection strength.

7.1 Recommendations for Future Research

Silicon photonic integrated circuits (PIC's) are intriguing subjects for exploration in their own right, but the impetus for investigating silicon photonics comes mainly from the vision of optoelectronics: the integration of optics and electronics on the same substrate. The resulting chips are called optoelectronic integrated circuits (OEIC's), and well designed OEIC will have performance and functionality greater than those of the optical and electrical circuits taken alone.

An electrically controlled filter for the selection of channels in DWDM optical network can be proposed to be the future research work. [28] In addition to gratings on top of a Rib waveguide, a forward biased P-i-N diode can be fabricated across the Rib, as Figure 7-1. Therefore, the wavelength selectivity is obtained by free carrier injection.

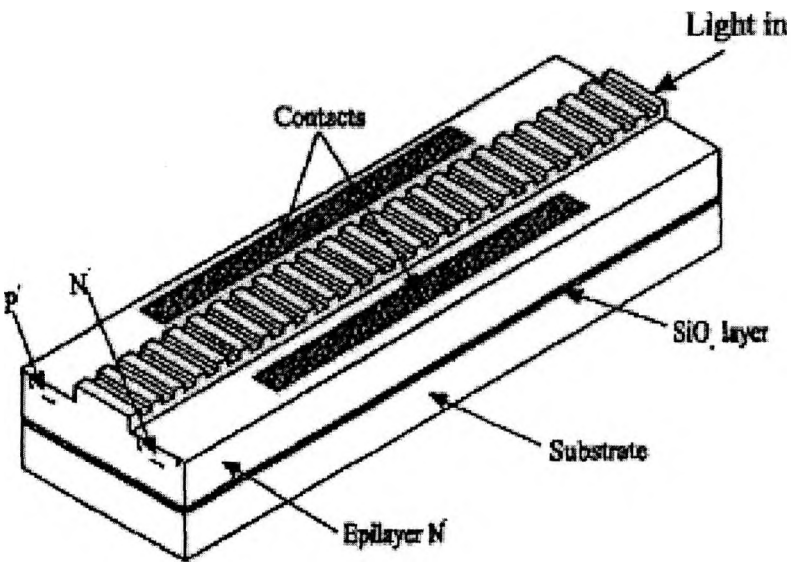

Figure 7-1 3D View of a Tunable Filter

Another potential future project can be explored is grating integrated Mach-Zehnder interferometer [29] as Figure 7-2. For certain wavelength that satisfies the Bragg condition of grating, the wavelength will get reflected and the output signal will be zero. Moreover, we can further utilize this wavelength to realize add/drop multiplexer. The ability to integrate Mach-Zehnder interferometer and gratings in this way without the need for any old fabrication trimming or adjustment could prove to be a good selling point for integrated Bragg gratings filters.

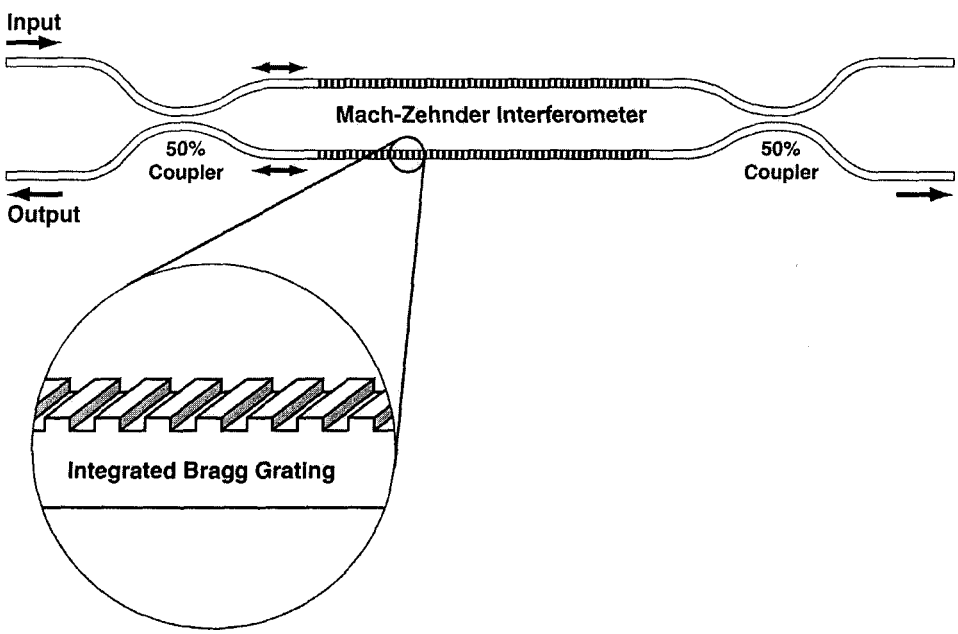

Figure 7-2 Grating Integrated Mach Zehnder Interferometer

Furthermore, more experimental and theoretical investigation of these devices could lead to a design which has little or no birefringence. Another limitation of this material system is the polarization dependence of perturbation. One solution to this problem would be to corrugate the sidewalls of the structure in addition to the top surface, in order to balance the TE and TM feedback. Since we neglected the

longitudinal field component E_z of TM modes when computing the overlap integral, more theoretical work should be done to investigate the coupling coefficient for the TM polarization.

Finally, much can be done to optimize the spectral response of a Bragg grating by intentionally introducing chirp and apodization. One way to achieve apodization is to adjust the lateral extent of the grating, by making the grating only cover part of the waveguide rather than the entire waveguide. Another way would be to adjust the depth of the grating across the device. For Bragg gratings formed by physical corrugations, the process of apodization invariably changes the effective index of the waveguide. For this reason, apodization and chirp are inextricably tied together. There are two ways to construct a filter with pure apodization. One way is to modify the waveguide width in tandem with the apodization profile such that the effective index of the waveguide remains constant. Another approach would be to intentionally chirp the grating in addition to apodization in order to compensate for the change in effective index induced by the apodization.

It is my hope that this thesis provides useful information to encourage others to develop new creative applications.

Appendix A

Matlab Source Codes

1. Simulation of Transmission Spectrum of 2.2 um SOI Waveguide

```
display('START');
format long;

%Index
nc=1;
nf=3.5;
ns=1.5;


%Grating Pitch
gpitch=220e-9

%Wavelength Range
wr=linspace(1400e-9,1600e-9,200);

%Grating height
a=0.08e-6

%SOI Si Thickness
thick=2.2e-6;

%Loop

for lambda_scan=1500e-9:1e-9:1600e-9

syms neff
 m=0;
 pi=3.1415926;
 k0=2*pi/lambda_scan;
 gammac=k0.*sqrt(neff^2-nc^2);
 kx=k0.*sqrt(nf^2-neff^2);
 gammas=k0.*sqrt(neff^2-ns^2);
 neff=solve(kx.*thick-(m+1)*pi+atan(kx./gammas)+atan(kx./gammac));
 neff=abs(double(neff));
 fun=neff;

  for m=0:8
     pi=3.1415926;
     neff=solve(kx.*thick-(m+1)*pi+atan(kx./gammas)+atan(kx./gammac));
     neff=abs(double(neff));

       if (abs(abs(neff*k0)+abs(fun*k0)-2*pi/gpitch)<1e4)
```

```
%Calculation of kappa
 k=2*(m+1)*pi^2./(3.*lambda_scan).*((nf^2-
nc^2)/nf).*(a/thick)^3.*(1+3/(2*pi).*lambda_scan./(a.*sqrt(nf^2-
nc^2))+3/4/pi/pi.*lambda_scan.*lambda_scan./(nf^2-nc^2)/a/a);


%Parameters
beta0=pi/gpitch;
beta=2*pi*abs(double(neff))./wr;
deltra_beta=beta-beta0;
s=sqrt(k^2-(deltra_beta.*deltra_beta));

%Grating Length
length=1e-2;

%Numerator
rho1=i.*s*exp(-i*beta0*length);

%Deumerator
rho2=exp(-i.*beta*length).*(-deltra_beta.*sinh(s.*length)+i.*s.*cosh(s.*length));

%Teff
t=rho1./rho2;

%Display
figure(1)
hold on
title('Transmission Spectrum');
xlabel('Wavelength(um)');
ylabel('Transmission');
legend('pitch=220nm');
plot(wr,abs(t).*abs(t),'b');


    end

   end


end
```

2. Variation of grating depth on 2.2 um SOI waveguide

```
%Wavelength Range
lambda_scan=linspace(1.5e-6,1.6e-6);

%Index
nc=1;
nf=3.5;
ns=1.5;

%SOI Si Thickness
thick=2.2e-6;


%Grating height
a=0.06e-6

%Calculation of kappa
lambda=1.55e-6;
k=2*pi^2./(3.*lambda).*((nf^2-
nc^2)/nf).*(a/thick)^3.*(1+3/(2*pi).*lambda./(a.*sqrt(nf^2-
nc^2))+3/4/pi/pi.*lambda.*lambda./(nf^2-nc^2)/a/a);


%Parameters
beta0=pi/0.224e-6;
beta=2*pi*3.48./lambda_scan;
deltra_beta=beta-beta0;
s=sqrt(k^2-(deltra_beta.*deltra_beta));

%Length
length=1e-2;

%Numerator
rho1=i.*s*exp(-i*beta0*length);

%Deumerator
rho2=exp(-i.*beta*length).*(-deltra_beta.*sinh(s.*length)+i.*s.*cosh(s.*length));

%Teff
t=rho1./rho2;

%Display
figure(1);
plot(lambda_scan,abs(t).*abs(t),'b');
title('Simulation of Grating Depth Effect');
xlabel('Wavelength(um)');
ylabel('Transmission');

%Grating height
a=0.07e-6
```

```
%Calculation of kappa
lambda=1.55e-6;
k=2*pi^2./(3.*lambda).*((nf^2-
nc^2)/nf).*(a/thick)^3.*(1+3/(2*pi).*lambda./(a.*sqrt(nf^2-
nc^2))+3/4/pi/pi.*lambda.*lambda./(nf^2-nc^2)/a/a);

%Parameters
beta0=pi/0.224e-6;
beta=2*pi*3.48./lambda_scan;
deltra_beta=beta-beta0;
s=sqrt(k^2-(deltra_beta.*deltra_beta));

%Length
length=1e-2;

%Numerator
rho1=i.*s*exp(-i*beta0*length);

%Deumerator
rho2=exp(-i.*beta*length).*(-deltra_beta.*sinh(s.*length)+i.*s.*cosh(s.*length));

%Teff
t=rho1./rho2;

%Display
figure(1)
hold on
plot(lambda_scan,abs(t).*abs(t),'r');
hold off

%Grating height
a=0.08e-6

%Calculation of kappa
lambda=1.55e-6;
k=2*pi^2./(3.*lambda).*((nf^2-
nc^2)/nf).*(a/thick)^3.*(1+3/(2*pi).*lambda./(a.*sqrt(nf^2-
nc^2))+3/4/pi/pi.*lambda.*lambda./(nf^2-nc^2)/a/a);

%Parameters
beta0=pi/0.224e-6;
beta=2*pi*3.48./lambda_scan;
deltra_beta=beta-beta0;
s=sqrt(k^2-(deltra_beta.*deltra_beta));

%Length
length=1e-2;

%Numerator
```

```
rho1=i.*s*exp(-i*beta0*length);

%Deumerator
rho2=exp(-i.*beta*length).*(-deltra_beta.*sinh(s.*length)+i.*s.*cosh(s.*length));

%Teff
t=rho1./rho2;

%Display
figure(1)
hold on
plot(lambda_scan,abs(t).*abs(t),'g');
hold off
```

References

[1] P.W.Shumate, "The Broadest Broadband Fiber to the Home," Scientific American, 281 (4), 104-105,1999.

[2] S.E. Miller, "Integrated Optics: An introduction" Bell Syst. Tech. J., pp 2059-2069, Sept 1969.

[3] Christina Manolatou, Hermann A. Haus, "Passive Components for Dense Optical Integration", Kluwer Academic Publishers, 2002.

[4] S. L. Chuang, "Physics of Optoelectronic Devices", Wiley-Interscience, 1995.

[5] Amnon Yariv, "Optical Electronics", 4th edition, Saunders College Publishing.

[6] Donald L. Lee, "Electromagnetic Principles of Integrated Optics", pp 93-94, John Wiley & Sons, Inc.

[7] R. A. Soref and J. P. Lorenzo, "All-silicon active and passive guided-wave components for λ=1.3 and 1.6um," IEEE J. Quantum Electron., vol 22, pp. 873- 879, 1986.

[8] B.N. Kurdi and D. G. Hall, "Optical waveguides in oxygen-implanted buried-oxide silicon-on-insulator structures," Opt Lett., vol. 13, pp. 175-177,1988.

[9] R. A Soref, J. Schmidtchen, and K. Petermann, "Large single-mode rib waveguides in GeSi-Si and Si-on-SiO_2," IEEE J. Quantum Electron., Vol. 27, pp. 1971-1974, Aug 1991.

[10] S. P. Pogossian, L. Vescan, and A. Vonsovici, " The single mode condition for semiconductor rib waveguides with large cross section," J. Lightwave Technol., vol.16, pp. 1851-1853, Oct 1998.

[11] A. G. Rickman, G. T. Reed, and F. Namavar, "Silicon-on-insulator rib waveguide loss and mode characteristics," J. Lightwave Technol., Vol 12, pp. 1771-1776, Oct 1994.

[12] Dietrich Marcuse, "Theory of dielectric optical waveguides", 2nd edition, Academic Press, Inc.

[13] Optiwave Company Inc., <http://www.optiwave.com/2003/products/optibpm/index.htm>

[14] A. Splett, M. Majd, and K. Petermann, " A novel beam propagation method for large refractive index steps and large propagation distances," IEEE Photo. Technol. Lett., vol. 3 pp. 274-276, Mar. 1991.

[15] Apollo Photonics Inc., < http://www.apollophoton.com> May 2003

[16] Yariv, A., and M. Nakamura, "Periodic structures for integrated optics," IEEE Quantum Electron., vol. QE-13, no.4, 1977.

[17] Suhara, T., and H.Nishihara, "Integrated optics components and devices using periodic structures," IEEE J. Quantum Electron., vol. QE-22, no 6, 1986.

[18] F.L Pedrotti and L.S. Pedrotti, "Introduction to Optics," 2nd edition, Prentice-Hall, 1993.

[19] Thomas E. Murphy, Jeffrey T. Hastings, Henry I. Smith, " Fabrication and Characterization of Narrow Band Bragg Refection Filters in Silicon on Insulator Ridge Waveguides," IEEE J. of Lightwave Technology, 2001.

[20]Wa Peng Wong, Kin Seng Chiang, "Desing of Polarization Insensitive Bragg Gratings in Zero Birefringence Ridge Waveguides," IEEE J. of Quantum Electronics, Vol. 37, No 9 September 2001.

[21] W. B. Joyce, B. C. DeLoach, "Alignment of Gaussian Beams", Appl. Opt., vol. 23, no. 23 Dec 1984.

[22] C. K. Tang, G. T. Reed, A. J. Walton, "Low Loss, Single Mode, Optical Phase Modulator in SIMOX Material," IEEE J. of Lightwave Technology,Vol.12 No8, August 1994.

[23] Jin Hong , W.P. Huang, "Countra-directional Coupling in Grating-Assisted Guided Wave Devices," IEEE Log Number 9108291.

[24] W.P. Huang, B. E. Little, C.L. Xu, "On Phase Matching and Power Coupling in Grating Assisted Coupers," IEEE Photonics Technology Letters, Vol. 4, No .2. February 1992.

[25] A. Cutolo, M.Iodice, A.Irace, P.Spirito, L.Zeni, "An electrically controlled Bragg refector integrated in a rib Silicon on insulator waveguide," Appl. Phys. Lett 71(2), July 1997.

[26] Vipul Rastogi, Kin Seng Chiang, "Long Period Gratings in Planar Optical Waveguides," Applied Optics, vol.41 No. 30 October 2002.

[27] B. Jalali, S. Yegnanarayanan, T. Yoon, T. Yoshimoto, I Rendna, F. Coppinger, "Advances in Silicon on Insulator Optoelectronics," IEEE J. of Quantum Electronics, Vol 4. No. 6, December 1998.

[28] A. Irace, G. Breglio, A. Cutolo, "All Silicon Optoelectronic Modulator with 1GHz Sitching Cpability," Electronics Letters, Vol. 39 No 2, January 2003.

[29] Richard A. Soref, "Silicon Based Optoelectronics," Proceedings of the IEEE, Vol 81 No. 12 December 1993